Isogeometric fluid–structure interaction analysis with emphasis on non-matching discretizations, and with application to wind turbines

Yuri Bazilevs[a,*], Ming-Chen Hsu[a], and Michael A. Scott[b]

[a]*Department of Structural Engineering, University of California, San Diego, 9500 Gilman Drive, Mail Code 0085, La Jolla, CA 92093, USA*
[b]*Institute for Computational Engineering and Sciences, The University of Texas at Austin, 1 University Station C0200, Austin, TX 78712, USA*

Abstract

In this paper we develop a framework for fluid–structure interaction (FSI) modeling and simulation with emphasis on Isogeometric Analysis (IGA) and non-matching fluid–structure interface discretizations. We take the augmented Lagrangian approach to FSI as a point of departure. Here the Lagrange multiplier field is defined on the fluid–structure interface and is responsible for coupling of the two subsystems. Thus the FSI formulation does not rely on the continuity of the underlying function spaces across the fluid–structure interface in order to produce the correct coupling conditions between the fluid and structural subdomains. However, in deriving the final FSI formulation the interface Lagrange multiplier is formally eliminated and the formulation is written purely in terms of primal variables. Avoiding the use of Lagrange multipliers adds efficiency to the proposed formulation. As an added benefit, the ability to employ non-matching grids for multi-physics simulations leads to significantly relaxed requirements that are placed on the geometry modeling and meshing tools for IGA.

We show an application of the proposed FSI formulation to the simulation of the NREL 5MW offshore wind turbine rotor, where the aerodynamics domain is modeled using volumetric quadratic NURBS, while the rotor structure is modeled using a cubic T-spline-based discretization of a rotation-free Kirchhoff–Love shell. We conclude the article by showing FSI coupling of a T-spline shell with a low-order Finite Element Method (FEM) discretization of the aerodynamics equations. This combined use of IGA and FEM is felt to be a good balance between speed, robustness, and accuracy of FSI simulations for this class of problems.

Keywords: Isogeometric Analysis, NURBS, T-splines, finite elements, multi–physics simulation, fluid–structure interaction, NREL 5MW offshore wind turbine rotor, aerodynamics, ALE–VMS, weakly enforced essential boundary conditions, Kirchhoff–Love rotation-free shell, non-matching interface discretizations

*Corresponding author
Email address: yuri@ucsd.edu (Y. Bazilevs)

The final publication is available at Elsevier via http://dx.doi.org/10.1016/j.cma.2012.03.028

1. Introduction

Isogeometric Analysis (IGA) [1, 2], despite its young age, has significantly matured as a technology for geometry representation and computational analysis.

NURBS remain a standard tool for geometry modeling in CAD (Computer Aided Design) and IGA. T-splines [3, 4] were introduced in the CAD community as a superior alternative to NURBS allowing for local mesh refinement and the representation of geometry of arbitrary topological genus, both of which are not possible with NURBS, but are critical for IGA. Since that time, T-splines have been applied successfully in the context of IGA [5–8] and have been enhanced to meet the demands of analysis [9, 10]. Advances in model quality definition and improvement enable the generation of better parameterized shapes for IGA, thus improving the quality of the computational solutions [11, 12]. Recent efforts to define standardized file formats for data exchange between geometry modeling and computational analysis software enabled straightforward solution of complicated structural problems that involve large deformation, plasticity and contact, using well-validated commercial FEM software [13–17]. Furthermore, IGA is able to elegantly handle many applications that otherwise create significant challenges to standard finite element technology [18–20].

However, several challenges remain for IGA to be fully accepted as industrial-strength analysis technology. The ability to create 3D volumetric complex geometry models in an automated manner is one such challenge. Another challenge is to prove that IGA is capable of producing accurate and robust results for complex-geometry multi-physics problems (e.g., fluid–structure interaction), which is one of the major demands of modern computational analysis.

This paper focuses on the coupling strategies, specific to IGA, for multi-physics applications. In particular, we consider fluid–structure interaction (FSI), which is an important representative of this class of problems. We focus on and formulate computational approaches for IGA that make use of non-matching discretizations of the domain geometry at the interface between the fluid and structure subdomains. Such coupling procedures allow greater flexibility in the computational analysis, and alleviate the difficulties of geometry modeling arising from the necessity to construct matching multi-physics interface discretizations. Furthermore, the mesh resolution of the structure and fluid mechanics problems may be tailored to the analysis requirements of the individual subsystems, leading to improved computational efficiency.

The increased complexity of structural geometry places heavy demands on the fluid volume mesh (or exterior mesh) generation around that structure. Generation of volumetric meshes for IGA has been successful in a handful of applications [21], including wind turbine modeling in [22]. However, no automatic mesh generation software for IGA exists to this day. Volumetric geometry modeling and mesh generation for IGA is, at this point, an active area of research that is still in its infancy (see [23, 24] for recent results for this challenging problem). As a result, in order to take advantage of the superior accuracy of IGA for structural mechanics applications (see, e.g., [25, 26]), and to leverage the existing advanced volumetric mesh generation tools for standard finite elements, we propose to couple FEM for fluid mechanics and IGA for structural dynamics. Although IGA was shown to produce results that are of better per-degree-of-freedom quality than standard FEM for fluid mechanics and, especially, for turbulent flows [27], good-quality aerodynamics may still be achieved with standard low-order FEM, with a manageable

number of degrees of freedom. Such results were presented in [28–30] for several cases of wind turbine aerodynamics simulations at full scale. We also feel this particular combination of FEM and IGA has the highest potential for near-term adoption by (and, as a result, for broader impact on) industry and national laboratories.

In this paper we propose an FSI methodology based on the augmented Lagrangian concept. We formally eliminate the Lagrange multiplier on the fluid–structure interface to achieve a formulation purely in terms of the primal variables (i.e., velocity and pressure for the fluid and velocity for the structural problem). The fluid and structural mechanics trial and test functions are not assumed to be equal at the interface, and the FSI coupling is taken care of in the variational formulation. This presents a convenient point of departure for a discrete FSI formulation using non-matching fluid-structure interface discretizations. In the non-matching FSI formulation one needs a functional definition of the kinematic quantities (velocity, displacement, etc.) and tractions on the fluid and structure meshes, and the ability to transfer these quantities from one mesh to the other. The L^2-projection is chosen in this work for the transfer of kinematic and traction data between the subdomains. It is found to be convenient from the standpoint of computer implementation. However, this procedure does not guarantee discrete momentum and energy conservation for non-matching discretizations. For a conservative approach to motion and load transfer in FSI, see [31].

We demonstrate an application of the proposed framework and methodology to FSI modeling and simulation of wind turbine rotors. The benefits of using IGA for this application were discussed in [22], and the importance of FSI modeling for this class of problems was demonstrated in [32]. In the aforementioned articles a model of a 5MW offshore wind turbine rotor defined in [33] was simulated and the results for quantities of engineering interest such as the aerodynamic torque and tip deflection were consistent with the findings of other researchers [22, 28, 29, 32–35] who simulated the same design numerically. To validate the aerodynamics procedures employed in this work, a smaller (20kW) rotor from [36] was simulated in [30], with very good matching between the experimental data and simulation results for the aerodynamic (low-speed shaft) torque and blade cross-section pressure distribution. In this work, we only consider the 5MW rotor, in part due to the fact that for large offshore wind turbine designs the blade deflections are considerable, and the FSI effects are significantly more pronounced.

This paper is outlined as follows.

In Section 2, we derive a family of FSI formulation at the continuous level using the augmented Lagrangian approach as a point of departure and formally eliminating the interface Lagrange multiplier. This leads to a set of FSI formulations, which are stated purely in terms of the primal variables.

In Section 3, we present the individual fluid and structural mechanics formulations at the discrete level, which are employed in the FSI computations presented in this paper. The equations of fluid mechanics make use of the residual-based variational multiscale (VMS) formulation of the Navier–Stokes equations [37] posed on a moving domain in the Arbitrary Lagrangian–Eulerian (ALE) frame. This fluid mechanics formulation is referred to as the ALE–VMS method. The ALE–VMS formulation is augmented with weakly enforced essential boundary conditions, which were first proposed in [38] and further improved and studied in [39–41].

The structural mechanics problem is governed by the rotation-free Kirchhoff–Love shell formulation, which was first proposed in [42], and further extended in [43] to the case of more complicated structural geometry, and in [32] to include dynamics and modeling of composite materials for FSI simulations of wind turbine rotors. We conclude this section with a discussion of the FSI coupling methodology employed in this work, as well as methods for kinematic and traction data transfer between non-matching fluid and structural subdomain discretizations.

In Section 4, we present the simulation results. We begin by performing standalone structural simulations of the NREL 5MW offshore wind turbine blade from [22, 33] subject to the aerodynamic traction (obtained from a separate aerodynamics computation from [35] using NURBS-based IGA) and centripetal forces. The aerodynamics traction vector was transferred to a matching bi-quadratic NURBS and a non-matching bi-cubic T-spline blade meshes. The relative difference in the tip deflection predicted by the matching and non-matching structural mechanics discretizations was less than 0.3%. We then perform an FSI simulation of the same wind turbine blade using the same wind conditions, rotor speed and NURBS mesh as in [32], however, the NURBS blade is now replaced with a T-Spline blade. Comparison of the FSI results using the matching and non-matching interface discretizations gave nearly identical results. Finally, as our last example, we present a computation of a T-spline blade coupled to a tetrahedral FEM fluid. In this case, all three rotor blades were simulated without invoking the assumption of rotational symmetry. The results are also in good agreement with prior IGA simulations, especially considering the coarseness of the aerodynamics FEM mesh.

In Section 5, we draw conclusions and outline future research directions.

2. FSI Formulation Based on the Augmented Lagrangian Approach

Let $(\Omega_1)_t \in \mathbb{R}^d$, $d = 2, 3$, represent the time-dependent domain of the fluid mechanics (or aerodynamics) problem, let $(\Omega_2)_t \in \mathbb{R}^d$ be the time-dependent domain of the structural mechanics problem, and let $(\Gamma_{\mathrm{I}})_t \in \mathbb{R}^d$ denote the interface between the fluid and structural domains. All the domains are taken at current time t at this point in the developments. Let $\mathbf{u}_1$ and p denote the fluid velocity and pressure, respectively. For the remainder of the article we assume that the fluid mechanics is governed by the Navier–Stokes equations of incompressible, isothermal, and Newtonian flow. Let $\mathbf{u}_2$ denote the velocity of the structure.

We define an augmented Lagrangian function $\mathbf{N}(\{\mathbf{u}_1, p\}, \mathbf{u}_2, \boldsymbol{\lambda})$ as

$$\begin{aligned}\mathbf{N}(\{\mathbf{u}_1, p\}, \mathbf{u}_2, \boldsymbol{\lambda}) = \mathbf{N}_1(\{\mathbf{u}_1, p\}) + \mathbf{N}_2(\mathbf{u}_2) \\ + \int_{(\Gamma_{\mathrm{I}})_t} \boldsymbol{\lambda} \cdot (\mathbf{u}_1 - \mathbf{u}_2)\, \mathrm{d}\Gamma \\ + \frac{1}{2} \int_{(\Gamma_{\mathrm{I}})_t} \beta(\mathbf{u}_1 - \mathbf{u}_2) \cdot (\mathbf{u}_1 - \mathbf{u}_2)\, \mathrm{d}\Gamma, \end{aligned} \tag{1}$$

where $\mathbf{N}_1$ and $\mathbf{N}_2$ are the Lagrangian functionals whose stationary points generate the variational equations of fluid and structural mechanics, $\boldsymbol{\lambda}$ is a Lagrange multiplier for the kinematic interface condition $\mathbf{u}_1 = \mathbf{u}_2$, and β is a penalty parameter, which we leave unspecified at the

moment. The augmented Lagrangian approach may be interpreted as a combination of the Lagrange multiplier and penalty methods. It is a popular approach in optimization, as well as in applications of nonlinear structural mechanics that involve some form of constraints (e.g., contact). Here, we adopt it as a point of departure for generating a family of FSI formulations.

Remark 1. The penalty term in Eq. (1) may be separated into normal and tangential velocity contributions. This option will be exploited in the next section. For simplicity of presentation, in this section, we keep this term in its original form.

Taking the variational derivatives of $\mathbf{N}$ with respect to the fluid, structural and Lagrange multiplier unknowns, and setting the result to zero, yields the following set of variational equations: Find the fluid velocity and pressure, $\mathbf{u}_1 \in \mathcal{S}_u$ and $p \in \mathcal{S}_p$, the structural velocity, $\mathbf{u}_2 \in \mathcal{S}_d$, and the Lagrange multiplier $\boldsymbol{\lambda} \in \mathcal{S}_l$, such that for all weighting functions $\mathbf{w}_1 \in \mathcal{V}_u$, $q_1 \in \mathcal{V}_p$, $\mathbf{w}_2 \in \mathcal{V}_d$, and $\delta\boldsymbol{\lambda} \in \mathcal{V}_l$

$$B_1(\{\mathbf{w}_1, q\}, \{\mathbf{u}_1, p\}) - F_1(\{\mathbf{w}_1, q\}) + \int_{(\Gamma_1)_t} \mathbf{w}_1 \cdot \boldsymbol{\lambda} \, \mathrm{d}\Gamma + \int_{(\Gamma_1)_t} \mathbf{w}_1 \cdot \beta(\mathbf{u}_1 - \mathbf{u}_2) \, \mathrm{d}\Gamma = 0, \tag{2}$$

$$B_2(\mathbf{w}_2, \mathbf{u}_2) - F_2(\mathbf{w}_2) - \int_{(\Gamma_1)_t} \mathbf{w}_2 \cdot \boldsymbol{\lambda} \, \mathrm{d}\Gamma - \int_{(\Gamma_1)_t} \mathbf{w}_2 \cdot \beta(\mathbf{u}_1 - \mathbf{u}_2) \, \mathrm{d}\Gamma = 0, \tag{3}$$

$$\int_{(\Gamma_1)_t} \delta\boldsymbol{\lambda} \cdot (\mathbf{u}_1 - \mathbf{u}_2) \, \mathrm{d}\Gamma = 0, \tag{4}$$

where $\mathcal{S}_u$, $\mathcal{S}_p$, $\mathcal{S}_d$, and $\mathcal{S}_l$ are the function spaces for the fluid velocity and pressure, structural velocity, and the Lagrange multiplier solutions, respectively, and $\mathcal{V}_u$, $\mathcal{V}_p$, $\mathcal{V}_d$, and $\mathcal{V}_l$ are the corresponding weighting function spaces. B_1, B_2, F_1, and F_2 are the semilinear forms and linear functional corresponding to the fluid and structural mechanics problems, respectively, and are given by:

$$\begin{aligned} B_1(\{\mathbf{w}, q\}, \{\mathbf{u}, p\}) = &\int_{(\Omega_1)_t} \mathbf{w} \cdot \rho_1 \left(\left.\frac{\partial \mathbf{u}}{\partial t}\right|_x + \mathbf{u} \cdot \boldsymbol{\nabla}_x \mathbf{u} \right) \mathrm{d}\Omega \\ &+ \int_{(\Omega_1)_t} \boldsymbol{\varepsilon}(\mathbf{w}) \ : \ \boldsymbol{\sigma}_1(\mathbf{u}, p) \ \mathrm{d}\Omega + \int_{(\Omega_1)_t} q \boldsymbol{\nabla}_x \cdot \mathbf{u} \, \mathrm{d}\Omega, \end{aligned} \tag{5}$$

$$F_1(\{\mathbf{w}, q\}) = \int_{(\Omega_1)_t} \mathbf{w} \cdot \rho_1 \mathbf{f} \, \mathrm{d}\Omega + \int_{(\Gamma_{1\mathrm{h}})_t} \mathbf{w} \cdot \mathbf{h} \, \mathrm{d}\Gamma, \tag{6}$$

$$B_2(\mathbf{w}, \mathbf{u}) = \int_{(\Omega_2)_t} \mathbf{w} \cdot \rho_2 \left.\frac{\partial \mathbf{u}}{\partial t}\right|_X \mathrm{d}\Omega + \int_{(\Omega_2)_t} \boldsymbol{\varepsilon}(\mathbf{w}) \ : \ \boldsymbol{\sigma}_2(\mathbf{u}) \, \mathrm{d}\Omega \tag{7}$$

$$F_2(\mathbf{w}) = \int_{(\Omega_2)_t} \mathbf{w} \cdot \rho_2 \mathbf{f} \, \mathrm{d}\Omega + \int_{(\Gamma_{2\mathrm{h}})_t} \mathbf{w} \cdot \mathbf{h} \, \mathrm{d}\Gamma, \tag{8}$$

where ρ_1 and ρ_2 are the fluid and structural densities, $\mathbf{f}$ and $\mathbf{h}$ are the applied body force and surface traction, $\big|_x$ denotes the fact that the time derivative in the fluid mechanics equations is taken with respect to the fixed coordinates of the spatial configuration, while $\big|_X$ in the structural problem denotes the fact that the time derivative is taken with respect to the fixed coordinates of the material configuration. The fluid Cauchy stress $\boldsymbol{\sigma}_1$ is given by

$$\boldsymbol{\sigma}_1(\mathbf{u}, p) = -p\mathbf{I} + 2\mu\boldsymbol{\varepsilon}(\mathbf{u}), \tag{9}$$

where $\mathbf{I}$ is the identity tensor, μ is the fluid dynamic viscosity, and $\boldsymbol{\varepsilon}(\mathbf{u})$ is the strain-rate tensor given by

$$\boldsymbol{\varepsilon}(\mathbf{u}) = \frac{1}{2}\left(\boldsymbol{\nabla}_x\mathbf{u} + \boldsymbol{\nabla}_x\mathbf{u}^T\right). \tag{10}$$

At this point we do not detail the structural Cauchy stress $\boldsymbol{\sigma}_2$ as we wish to keep the structural mechanics formulation as flexible as possible.

The variational formulations given by Eqs. (2)–(3) give the following Euler–Lagrange conditions on the fluid-structural interface $(\Gamma_I)_t$:

$$\boldsymbol{\lambda} = -\boldsymbol{\sigma}_1\mathbf{n}_1 - \beta(\mathbf{u}_1 - \mathbf{u}_2), \tag{11}$$

$$\boldsymbol{\lambda} = \boldsymbol{\sigma}_2\mathbf{n}_2 - \beta(\mathbf{u}_1 - \mathbf{u}_2), \tag{12}$$

where $\mathbf{n}_1$ and $\mathbf{n}_2$ are the unit outward normal vectors to the fluid and structural domains, respectively. Note that, at the fluid–structure interface, $\mathbf{n}_1 = -\mathbf{n}_2$. Subtracting Eq. (11) from Eq. (12) results in

$$\boldsymbol{\sigma}_1\mathbf{n}_1 + \boldsymbol{\sigma}_2\mathbf{n}_2 = \mathbf{0}, \tag{13}$$

which the fluid and structure tractions are in equilibrium at their interface. The Lagrange multiplier Eq. (4) implies the kinematic compatibility condition at the fluid–structure interface, namely

$$\mathbf{u}_1 = \mathbf{u}_2. \tag{14}$$

Remark 2. Note that the traction compatibility condition given by Eq. (13) was derived without using the kinematic compatibility condition $\mathbf{u}_1 = \mathbf{u}_2$. This is a consequence of the augmented Lagrangian formulation.

Introducing Eq. (14) into Eqs.(11)–(12) yields

$$\boldsymbol{\lambda} = -\boldsymbol{\sigma}_1\mathbf{n}_1 = \boldsymbol{\sigma}_2\mathbf{n}_2, \tag{15}$$

which gives an interpretation of the Lagrange multiplier as the interface traction vector that may be computed from the fluid or structural subdomains. As a result, $\boldsymbol{\lambda}$ may be expressed as convex combination of the fluid and structure traction vectors as

$$\boldsymbol{\lambda} = -\alpha\boldsymbol{\sigma}_1\mathbf{n}_1 + (1-\alpha)\boldsymbol{\sigma}_2\mathbf{n}_2, \tag{16}$$

where α is a real number.

We now formally eliminate the Lagrange multiplier from the formulation of the FSI problem. The variation of $\boldsymbol{\lambda}$ with respect to the fluid and structural mechanics unknowns may be computed directly from Eq. (16), which gives

$$\delta\boldsymbol{\lambda} = -\alpha\delta_{\{\mathbf{u}_1,p\}}\boldsymbol{\sigma}_1\mathbf{n}_1(\{\mathbf{w}_1,q\}) + (1-\alpha)\delta_{\mathbf{u}_2}\boldsymbol{\sigma}_2\mathbf{n}_2(\mathbf{w}_2). \tag{17}$$

Introducing Eqs. (16)–(17) into Eqs. (2)–(4), scaling Eq.(4) by the parameter γ, and combining Eqs. (2)–(4) into a single variational form gives: find $\mathbf{u}_1 \in \mathcal{S}_u$, $p \in \mathcal{S}_p$, and $\mathbf{u}_2 \in \mathcal{S}_d$, such that for all $\mathbf{w}_1 \in \mathcal{V}_u$, $q_1 \in \mathcal{V}_p$, and $\mathbf{w}_2 \in \mathcal{V}_d$

$$\begin{aligned}
&B_1(\{\mathbf{w}_1,q\},\{\mathbf{u}_1,p\}) - F_1(\{\mathbf{w}_1,q\}) + B_2(\mathbf{w}_2,\mathbf{u}_2) - F_2(\mathbf{w}_2)\\
&+\int_{(\Gamma_1)_t}(\mathbf{w}_1-\mathbf{w}_2)\cdot(-\alpha\boldsymbol{\sigma}_1\mathbf{n}_1+(1-\alpha)\boldsymbol{\sigma}_2\mathbf{n}_2)\ \mathrm{d}\Gamma\\
&+\gamma\int_{(\Gamma_1)_t}\Big(-\alpha\delta_{\{\mathbf{u}_1,p\}}\boldsymbol{\sigma}_1\mathbf{n}_1(\{\mathbf{w}_1,q\})+(1-\alpha)\delta_{\mathbf{u}_2}\boldsymbol{\sigma}_2\mathbf{n}_2(\mathbf{w}_2)\Big)\cdot(\mathbf{u}_1-\mathbf{u}_2)\ \mathrm{d}\Gamma\\
&+\int_{(\Gamma_1)_t}(\mathbf{w}_1-\mathbf{w}_2)\cdot\beta(\mathbf{u}_1-\mathbf{u}_2)\ \mathrm{d}\Gamma = 0.
\end{aligned} \tag{18}$$

The variational statement given by Eq. (18) defines a family of FSI formulations parameterized by α, β and γ. However, we note that the different choices of these parameters do not change the underlying FSI problem.

In this work we choose $\alpha = 1$ and $\gamma = 1$. The former choice is motivated by the fact that here we wish to avoid taking a variation of the structural Cauchy stress, while the latter choice leads to adjoint consistency of our discrete formulation (see [44] for details). We postpone the choice of β until we state the discrete FSI problem.

With this definition of the parameters, we obtain the following coupled formulation: find $\mathbf{u}_1 \in \mathcal{S}_u$, $p \in \mathcal{S}_p$, and $\mathbf{u}_2 \in \mathcal{S}_d$, such that for all $\mathbf{w}_1 \in \mathcal{V}_u$, $q_1 \in \mathcal{V}_p$, and $\mathbf{w}_2 \in \mathcal{V}_d$

$$\begin{aligned}
&B_1(\{\mathbf{w}_1,q\},\{\mathbf{u}_1,p\}) - F_1(\{\mathbf{w}_1,q\}) + B_2(\mathbf{w}_2,\mathbf{u}_2) - F_2(\mathbf{w}_2)\\
&-\int_{(\Gamma_1)_t}(\mathbf{w}_1-\mathbf{w}_2)\cdot\boldsymbol{\sigma}_1\mathbf{n}_1\ \mathrm{d}\Gamma\\
&-\int_{(\Gamma_1)_t}\Big(\delta_{\{\mathbf{u}_1,p\}}\boldsymbol{\sigma}_1\mathbf{n}_1(\{\mathbf{w}_1,q\})\Big)\cdot(\mathbf{u}_1-\mathbf{u}_2)\ \mathrm{d}\Gamma\\
&+\int_{(\Gamma_1)_t}(\mathbf{w}_1-\mathbf{w}_2)\cdot\beta(\mathbf{u}_1-\mathbf{u}_2)\ \mathrm{d}\Gamma = 0.
\end{aligned} \tag{19}$$

The coupled formulation given by Eq. (19) leads to the following interpretation of the individual fluid and structural subproblems. The fluid subproblem may be obtained by setting $\mathbf{w}_2 = \mathbf{0}$. This yields: find $\mathbf{u}_1 \in \mathcal{S}_u$ and $p \in \mathcal{S}_p$ such that for all $\mathbf{w}_1 \in \mathcal{V}_u$ and $q_1 \in \mathcal{V}_p$

$$B_1(\{\mathbf{w}_1,q\},\{\mathbf{u}_1,p\}) - F_1(\{\mathbf{w}_1,q\})$$

$$
\begin{aligned}
&- \int_{(\Gamma_1)_t} \mathbf{w}_1 \cdot \boldsymbol{\sigma}_1 \mathbf{n}_1 \, \mathrm{d}\Gamma \\
&- \int_{(\Gamma_1)_t} \left(\delta_{\{\mathbf{u}_1, p\}} \boldsymbol{\sigma}_1 \mathbf{n}_1(\{\mathbf{w}_1, q\}) \right) \cdot (\mathbf{u}_1 - \mathbf{u}_2) \, \mathrm{d}\Gamma \\
&+ \int_{(\Gamma_1)_t} \mathbf{w}_1 \cdot \beta(\mathbf{u}_1 - \mathbf{u}_2) \, \mathrm{d}\Gamma = 0,
\end{aligned} \tag{20}
$$

where one immediately recognizes a continuous counterpart of the fluid mechanics formulation with weakly enforced essential boundary conditions on the fluid velocity [38]. These essential boundary conditions come from the structural velocity at the fluid–structure interface.

Setting $\{\mathbf{w}_1, q\} = \{\mathbf{0}, 0\}$ in Eq. (19) gives the following structural subproblem: find $\mathbf{u}_2 \in \mathcal{S}_d$, such that for all $\mathbf{w}_2 \in \mathcal{V}_d$

$$
B_2(\mathbf{w}_2, \mathbf{u}_2) - F_2(\mathbf{w}_2) + \int_{(\Gamma_1)_t} \mathbf{w}_2 \cdot \left(\boldsymbol{\sigma}_1 \mathbf{n}_1 + \beta \left(\mathbf{u}_2 - \mathbf{u}_1 \right) \right) \, \mathrm{d}\Gamma = 0, \tag{21}
$$

which states that at the fluid–structure interface the structural problem is driven by the fluid traction vector $\mathbf{t}_1$ given by

$$
\mathbf{t}_1 = -\boldsymbol{\sigma}_1 \mathbf{n}_1 - \beta \left(\mathbf{u}_2 - \mathbf{u}_1 \right) \tag{22}
$$

The traction vector contains the usual term $-\boldsymbol{\sigma}_1 \mathbf{n}_1$, and it is also augmented by the term that is proportional to the difference between the fluid and structural velocities at their interface.

Remark 3. Choosing $\alpha = 1$ in Eq. (18) leads to subproblems defined by Eqs. (20) and (21). With this choice, the fluid mechanics problem is responsible for satisfying the kinematic compatibility condition, while the structural subproblem is responsible for satisfying the traction compatibility condition. This interpretation is consistent with how one typically thinks about FSI problems. Other choices of α lead to different interpretations of the FSI problem. For example, setting $\alpha = 0$ reverses the roles of the fluid and structural subproblems in that now the structure is responsible for satisfying the kinematic compatibility condition and the fluid enforces the compatibility of tractions. Intermediate values of α lead to other interpretations of the roles played by the individual subproblems.

Remark 4. The coupled formulation given by Eq. (18), derived using the augmented Lagrangian approach as a starting point, may also be interpreted as Nitsche's method for FSI (see, e.g., [45, 46]) or as a continuous version of the Discontinuous Galerkin method for FSI applied at the fluid–structure interface.

Remark 5. In the above developments we assumed that the trial and test function spaces of the fluid and structural subproblems are independent of each other. This approach provides one with the framework that is capable of handling non-matching fluid and structural interface discretizations. If we explicitly assume that the fluid and structural velocities and the corresponding test functions are continuous at their interface, the FSI formulation given by Eq. (18) reduces to: find $\mathbf{u}_1 \in \mathcal{S}_u$, $p \in \mathcal{S}_p$, and $\mathbf{u}_2 \in \mathcal{S}_d$, such that for all $\mathbf{w}_1 \in \mathcal{V}_u$, $q_1 \in \mathcal{V}_p$, and $\mathbf{w}_2 \in \mathcal{V}_d$

$$
B_1(\{\mathbf{w}_1, q\}, \{\mathbf{u}_1, p\}) - F_1(\{\mathbf{w}_1, q\}) + B_2(\mathbf{w}_2, \mathbf{u}_2) - F_2(\mathbf{w}_2) = 0. \tag{23}
$$

This form of the FSI problem is suitable for matching fluid–structure interface meshes. Although somewhat limiting, matching interface discretizations were employed in [47–52] to solve several problems of contemporary interest in computational mechanics and engineering.

3. FSI Formulation for Non-Matching Discretizations Suitable for IGA and FEM

In this section we develop the coupled FSI formulation at the discrete level. We assume non-matching fluid–structure interface discretization and take the continuous fluid and structural formulations from the previous section as a point of departure. We present the fluid and structural mechanics problems separately, describe the fluid–structural coupling and present our kinematic and traction data transfer methods between the non-matching fluid and structural interface discretizations.

3.1. The ALE–VMS Formulation of Fluid Mechanics with Weak Boundary Conditions

We begin with the fluid mechanics problem given by Eq. (20), and state the corresponding semi-discrete variational formulation: find $\mathbf{u}_1^h \in \mathcal{S}_u^h$ and $p^h \in \mathcal{S}_p^h$ such that for all $\mathbf{w}_1^h \in \mathcal{V}_u^h$ and $q_1^h \in \mathcal{V}_p^h$

$$
\begin{aligned}
&B_1^{MS}(\{\mathbf{w}_1^h, q^h\}, \{\mathbf{u}_1^h, p^h\}) - F_1^{MS}(\{\mathbf{w}_1^h, q^h\}) \\
&- \sum_{b=1}^{N_{\text{eb}}} \int_{\Gamma^b \cap (\Gamma_1)_t} \mathbf{w}_1^h \cdot \boldsymbol{\sigma}_1\left(\mathbf{u}_1^h, p^h\right)\mathbf{n}_1 \, \mathrm{d}\Gamma \\
&- \sum_{b=1}^{N_{\text{eb}}} \int_{\Gamma^b \cap (\Gamma_1)_t} \left(2\mu\boldsymbol{\varepsilon}\left(\mathbf{w}_1^h\right)\mathbf{n}_1 + q^h\mathbf{n}_1\right) \cdot \left(\mathbf{u}_1^h - \hat{\mathbf{u}}^h\right) \, \mathrm{d}\Gamma \\
&- \sum_{b=1}^{N_{\text{eb}}} \int_{\Gamma^b \cap (\Gamma_1)_t^-} \mathbf{w}_1^h \cdot \rho_1 \left(\left(\mathbf{u}_1^h - \hat{\mathbf{u}}^h\right) \cdot \mathbf{n}_1\right)\left(\mathbf{u}_1^h - \hat{\mathbf{u}}^h\right) \, \mathrm{d}\Gamma \\
&+ \sum_{b=1}^{N_{\text{eb}}} \int_{\Gamma^b \cap (\Gamma_1)_t} \tau_{\text{TAN}}^B \left(\mathbf{w}_1^h - \left(\mathbf{w}_1^h \cdot \mathbf{n}_1\right)\mathbf{n}_1\right) \cdot \left(\left(\mathbf{u}_1^h - \hat{\mathbf{u}}^h\right) - \left(\left(\mathbf{u}_1^h - \hat{\mathbf{u}}^h\right) \cdot \mathbf{n}_1\right)\mathbf{n}_1\right) \, \mathrm{d}\Gamma \\
&+ \sum_{b=1}^{N_{\text{eb}}} \int_{\Gamma^b \cap (\Gamma_1)_t} \tau_{\text{NOR}}^B \left(\mathbf{w}_1^h \cdot \mathbf{n}_1\right)\left(\left(\mathbf{u}_1^h - \hat{\mathbf{u}}^h\right) \cdot \mathbf{n}_1\right) \, \mathrm{d}\Gamma = 0,
\end{aligned}
\tag{24}
$$

where B_1^{MS} and F_1^{MS} are the discrete counterparts of B_1 and F_1, respectively, given by

$$
\begin{aligned}
&B_1^{MS}(\{\mathbf{w}^h, q^h\}, \{\mathbf{u}^h, p^h\}) = \\
&\int_{(\Omega_1)_t} \mathbf{w}^h \cdot \rho_1 \left(\left.\frac{\partial \mathbf{u}^h}{\partial t}\right|_{\hat{x}} + \left(\mathbf{u}^h - \hat{\mathbf{u}}^h\right) \cdot \boldsymbol{\nabla}_x \mathbf{u}^h\right) \mathrm{d}\Omega + \int_{(\Omega_1)_t} \boldsymbol{\varepsilon}\left(\mathbf{w}^h\right) \, : \, \boldsymbol{\sigma}\left(\mathbf{u}^h, p^h\right) \, \mathrm{d}\Omega \\
&+ \int_{(\Omega_1)_t} q^h \boldsymbol{\nabla}_x \cdot \mathbf{u}^h \, \mathrm{d}\Omega \\
&+ \sum_{e=1}^{N_{\text{el}}} \int_{(\Omega_1^e)_t} \tau_{\text{SUPS}} \left(\left(\mathbf{u}^h - \hat{\mathbf{u}}^h\right) \cdot \boldsymbol{\nabla}_x \mathbf{w}^h + \frac{\boldsymbol{\nabla}_x q^h}{\rho_1}\right) \cdot \mathbf{r}_{\text{M}}\left(\mathbf{u}^h, p^h\right) \, \mathrm{d}\Omega
\end{aligned}
$$

$$
\begin{aligned}
&+ \sum_{e=1}^{N_{\text{el}}} \int_{(\Omega_1^e)_t} \rho_1 \nu_{\text{LSIC}} \boldsymbol{\nabla}_x \cdot \mathbf{w}^h r_{\text{C}}(\mathbf{u}^h, p^h) \, \mathrm{d}\Omega \\
&- \sum_{e=1}^{N_{\text{el}}} \int_{(\Omega_1^e)_t} \tau_{\text{SUPS}} \mathbf{w}^h \cdot \left(\mathbf{r}_{\text{M}} \left(\mathbf{u}^h, p^h \right) \cdot \boldsymbol{\nabla}_x \mathbf{u}^h \right) \, \mathrm{d}\Omega \\
&- \sum_{e=1}^{N_{\text{el}}} \int_{(\Omega_1^e)_t} \frac{\boldsymbol{\nabla}_x \mathbf{w}^h}{\rho_1} \, : \, \left(\tau_{\text{SUPS}} \mathbf{r}_{\text{M}} \left(\mathbf{u}^h, p^h \right) \right) \otimes \left(\tau_{\text{SUPS}} \mathbf{r}_{\text{M}} \left(\mathbf{u}^h, p^h \right) \right) \, \mathrm{d}\Omega,
\end{aligned} \tag{25}
$$

and

$$
F_1^{MS}(\{\mathbf{w}^h, q^h\}) = F_1(\{\mathbf{w}^h, q^h\}). \tag{26}
$$

The above formulation corresponds to an ALE–VMS method with weakly enforced essential boundary conditions. The discrete velocities and pressures and the corresponding test functions are now superscripted with h to denote their dependence on the mesh size. The Arbitrary Lagrangian–Eulerian (ALE) formulation is employed to handle the moving spatial domain of the fluid mechanics problem. Note that $\left|_{\hat{x}}\right.$ in Eq. (25) denotes the fact that the time derivative is taken with respect to a fixed referential domain spatial coordinates $\hat{\mathbf{x}}$, and $\hat{\mathbf{u}}^h$ is the mesh velocity. The time-dependent fluid domain $(\Omega_1)_t$ is divided into N_{el} individual element subdomains denoted by $(\Omega_1^e)_t$. The discrete trial function spaces $\mathcal{S}_u^h$ for the velocity and $\mathcal{S}_p^h$ for the pressure, as well as the corresponding test function spaces $\mathcal{V}_u^h$ and $\mathcal{V}_p^h$ are assumed to be of equal order, and, in this work, are comprised of NURBS or FEM functions. In Eq. (25), $\mathbf{r}_{\text{M}}$ and r_{C} are the residuals of the momentum and continuity (incompressibility constraint) equations, respectively, given by

$$
\mathbf{r}_{\text{M}}(\mathbf{u}^h, p^h) = \rho_1 \left(\left. \frac{\partial \mathbf{u}^h}{\partial t} \right|_{\hat{x}} + \left(\mathbf{u}^h - \hat{\mathbf{u}}^h \right) \cdot \boldsymbol{\nabla}_x \mathbf{u}^h - \mathbf{f}^h \right) - \boldsymbol{\nabla}_x \cdot \boldsymbol{\sigma}_1 \left(\mathbf{u}^h, p^h \right) \tag{27}
$$

and

$$
r_{\text{C}}(\mathbf{u}^h, p^h) = \boldsymbol{\nabla}_x \cdot \mathbf{u}^h, \tag{28}
$$

and τ_{SUPS} and ν_{LSIC} are the stabilization parameters, whose definition may be found in [37, 48, 53–60]).

The fluid–structure interface $(\Gamma_{\text{I}})_t$ is decomposed into N_{eb} fluid domain surface elements, and $(\Gamma_{\text{I}})_t^-$ is defined as the "inflow" part of $(\Gamma_{\text{I}})_t$ as

$$
(\Gamma_{\text{I}})_t^- = \left\{ \mathbf{x} \; \middle| \; \left(\mathbf{u}_1^h - \hat{\mathbf{u}}^h \right) \cdot \mathbf{n}_1 < 0, \; \forall \mathbf{x} \subset (\Gamma_{\text{I}})_t \right\}. \tag{29}
$$

The penalty parameter τ^B is, in general, assumed to be different for the slip and penetration components of the flow velocity. However, for the computations presented in this work we use the same definition for both, namely,

$$
\tau_{\text{TAN}}^B = \tau_{\text{NOR}}^B = \frac{C_I^B \mu_1}{h_n}, \tag{30}
$$

where h_n is the wall-normal element size, and C_I^B is a sufficiently large positive constant, which is computed from an appropriate element-level inverse estimate (see, e.g., [61–63]). For more details on weakly enforced boundary condition in fluid mechanics the reader is referred to [38–40]. The main advantage of this approach over strongly enforced boundary conditions is the added flexibility of the flow to slip on the solid surface in the case when the wall-normal mesh size is relatively large. This effect tends to produce more accurate fluid mechanics solutions than those coming from strongly enforced boundary conditions. See [30] for a recent successful application of weakly enforced boundary conditions in the validation of the ALE–VMS methodology for wind turbine aerodynamics at full scale.

Remark 6. The stabilization parameters τ_{SUPS} and ν_{LSIC} in the above equations originate from stabilized finite element methods for fluid dynamics (see, e.g., [53–59]). The stabilization parameters were designed and studied extensively in the context of stabilized finite element formulations of linear model problems of direct relevance to fluid mechanics. The design of τ_{SUPS} and ν_{LSIC} is such that optimal convergence with respect to the mesh size and polynomial order of discretization is attained for the cases of advection–diffusion, Stokes and Oseen equations (see, e.g., [59] and references therein). Furthermore, enhanced stability for advection-dominated flows and the ability to conveniently employ the same basis functions for velocity and pressure variables for incompressible flow are some of the attractive outcomes of this method. More recently, the stabilization parameters were derived in the context of the variational multiscale methods [64, 65] and were interpreted as the appropriate averages of the small-scale Green's function, a key mathematical object in the theory of VMS methods (see [66] for an elaboration). The ALE–VMS formulation is a moving-domain extension of the residual-based variational multiscale (RBVMS) turbulence modeling technique proposed for stationary domains in [37]. It was also presented in [48] for moving domains in the context of FSI. Recently, in [67], the authors extended the RBVMS formulation for moving domain problems using the space–time finite element method.

Remark 7. Rather than setting the no-slip boundary conditions exactly, the weak boundary condition formulation gives the no-slip solution only in the limit as $h_n \to 0$. As a result, coarse boundary layer discretizations do not need to struggle to resolve thin boundary layers; the flow simply slips on the solid boundary. Because of this added flexibility, the weak boundary condition enforcement approach tends to produce more accurate results on meshes that are too coarse to capture the boundary layer solution. However, as the mesh is refined to capture the boundary layer, both weak and strong boundary condition formulations produce nearly identical results (see [39]).

Remark 8. Although the weak boundary condition formulation is also stable for very large values of C_I^B, we do not advocate this choice. Large values of C_I^B place a heavy penalization on the no-slip condition, and the above mentioned flexibility of the method is lost together with the associated accuracy benefits. We advocate using C_I^B that is just large enough to guarantee the stability of the discrete formulation.

The mesh velocity $\hat{\mathbf{u}}^h$ in Eqs. (24)–(25) is obtained as follows. On the fluid–structure inter-

face $(\Gamma_1)_t$ the fluid domain mesh velocity $\hat{\mathbf{u}}^h$ is given by

$$\hat{\mathbf{u}}^h = \Pi_1^h \mathbf{u}_2^h, \tag{31}$$

where Π_1^h is a projection or interpolation operator onto the space spanned by the basis functions of the fluid mechanics problem restricted to the fluid–structure interface. In this work we use an L^2-projection. On the fluid mechanics domain interior the mesh velocity is obtained as a time derivative of an appropriate extension of the structural displacement on the fluid–structure boundary into the fluid domain interior. In the case of wind turbine simulations presented in this paper, the differential equations of elastostatics (subject to time-dependent boundary conditions) are employed to handle the deflection part of the rotor structural motion, while the rotational part of the rotor motion is handled exactly (see [32] for a precise mathematical formulation of this technique). For a variety of other mesh update strategies the reader is referred to [68–71]. Equation (31) couples the fluid mechanics problem to the structural mechanics problem, which is discussed in the next section.

To connect the discrete fluid mechanics formulation presented in this section to the continuous counterpart given by Eq. (20) in the previous section, we observe that: 1. The Galerkin terms are replaced with their ALE–VMS counterparts on the first line of Eq. (24); 2. The discrete counterpart of the variation of the fluid traction vector from the third line of Eq. (20) may be computed directly as

$$\delta_{\{\mathbf{u}_1^h, p^h\}} \boldsymbol{\sigma}_1 \mathbf{n}_1(\{\mathbf{w}_1^h, q^h\}) = 2\mu\boldsymbol{\varepsilon}(\mathbf{w}_1^h)\mathbf{n}_1 + q^h \mathbf{n}_1, \tag{32}$$

which motivates the third term in Eq. (24). However, note the sign change on the pressure test function, which is necessary for the pressure stability of the discrete formulation. The term on the fourth line of Eq. (24) is added to enhance the stability of the formulation on $(\Gamma_1)_t^-$. These enhancements do not violate consistency or adjoint consistency of the discrete formulation; 3. Finally, the penalty parameter β from the fourth line of Eq. (20) is set equal to τ^B. As a result, the penalty term of the augmented Lagrangian formulation directly translates to the penally term of the weakly enforced boundary conditions.

3.2. Rotation-Free Kirchhoff–Love Shell Formulation of Structural Mechanics

In this work, we use a shell formulation for the structural mechanics problem. We assume that the shell midsurface is described using a piece-wise smooth (C^1-continuous or smoother) geometrical mapping. We also allow regions where the mapping reduces to the C^0 level. We are thinking of situations where the surface geometry of the shell is described using several NURBS patches, which are "glued" together with C^0 continuity, or as a single or multiple T-spline surfaces, also with a possible continuity reduction. (For complex shell structures the geometry definition often requires that the continuity of the geometrical mapping is reduced to the C^0 level. Examples of such cases include a trailing edge of an airfoil or a I-beam, the latter being a non-manifold surface.) For this reason we define

$$(\Gamma_2)_0 = \bigcup_{i=1}^{N_{sp}} (\Gamma_2^i)_0, \tag{33}$$

$$(\Gamma_2)_t = \bigcup_{i=1}^{N_{sp}} (\Gamma_2^i)_t, \tag{34}$$

where $(\Gamma_2)_0$ and $(\Gamma_2)_t$ denote the structure midsurface in the reference and deformed configuration, respectively, $(\Gamma_2^i)_0$ and $(\Gamma_2^i)_t$, $i = 1, 2, \ldots, N_{sp}$, are the structural patches or subdomains in the reference and deformed configuration, respectively, and N_{sp} is their number. Following the procedures developed in [32, 42, 43], we state the discrete variational formulation of the rotation-free Kirchhoff–Love shell as: find the velocity of the shell midsurface $\mathbf{u}_2^h \in \mathcal{S}_d^h$, such that for all functions $\mathbf{w}_2^h \in \mathcal{V}_d^h$,

$$\begin{aligned}
&\int_{(\Gamma_2)_t} \mathbf{w}_2^h \cdot \rho_2 h_{th} \left(\left. \frac{\partial \mathbf{u}_2^h}{\partial t} \right|_{\mathbf{X}} - \mathbf{f} \right) \mathrm{d}\Gamma + \int_{(\Gamma_2)_0} \delta\overline{\boldsymbol{\epsilon}}^h \cdot \left(\mathbf{A}\overline{\boldsymbol{\epsilon}}^h + \mathbf{B}\overline{\boldsymbol{\kappa}}^h \right) \mathrm{d}\Gamma \\
&+ \int_{(\Gamma_2)_0} \delta\overline{\boldsymbol{\kappa}}^h \cdot \left(\mathbf{B}\overline{\boldsymbol{\epsilon}}^h + \mathbf{D}\overline{\boldsymbol{\kappa}}^h \right) \mathrm{d}\Gamma - \int_{(\Gamma_1)_t} \mathbf{w}_2^h \cdot (\Pi_2^h \mathbf{t}_1^h) \, \mathrm{d}\Gamma = 0.
\end{aligned} \tag{35}$$

In the above formulation h_{th} is the shell thickness, $\overline{\boldsymbol{\epsilon}}^h$ and $\overline{\boldsymbol{\kappa}}^h$ are the tensors of membrane strains and curvature changes, written in Voigt notation and with respect to the local Cartesian basis oriented on the first covariant basis vector of the midsurface, $\delta\overline{\boldsymbol{\epsilon}}^h$ and $\delta\overline{\boldsymbol{\kappa}}^h$ are their variations, and $\mathbf{A}$, $\mathbf{B}$, and $\mathbf{D}$ are the membrane, coupling and bending stiffnesses pre-integrated through the thickness.

The last term on the left-hand-side of Eq. (35) is the discrete counterpart of the fluid traction vector from Eq. (22) given by

$$\mathbf{t}_1^h = -\boldsymbol{\sigma}_1^h \mathbf{n}_1 - \tau^B \left(\hat{\mathbf{u}}^h - \mathbf{u}_1^h \right), \tag{36}$$

where the mesh velocity $\hat{\mathbf{u}}^h$ is obtained from the structural velocity $\mathbf{u}_2^h$ using Eq. (31), and Π_2^h is a projection or interpolation operator onto the space spanned by the basis functions of the structural mechanics problem restricted to the fluid–structure interface. Here, Π_2^h corresponds to the L^2-projector, which globally conserves forces and moments acting on the structure.

Kirchhoff–Love shell kinematics assumes that the shell director stays orthogonal to the shell midsurface during the motion, which eliminates transverse shear strains. Transverse shear stresses are also neglected in the theory. These assumptions are adequate provided the shell is sufficiently thin. While the formulation is able to accommodate large structural deformations, it is assumed that the stress-strain relationship is linear (i.e., the St. Venant–Kirchhoff material model is used). Composite materials, which are typically employed in the manufacturing of wind turbine blades, are modeled within this framework by homogenizing the structural material properties (density and stiffness) in the through-thickness direction. See [32] for more details.

Remark 9. It was shown in [35] that the use of thin shell theory is suitable for the current application in that the transverse shear effect is not playing an important role in predicting the deformation of the composite wind turbine blade under the combined action of centripetal, gravity, and aerodynamic loads.

The variational formulation given by Eq. (35) is valid over regions of the shell surface described by a smooth mapping. In the regions where the continuity of the mapping drops to the C^0 level, the formulation is no longer conforming. The Bending Strip Method, introduced in [43], overcomes this difficulty by adding a simple, physically-motivated penalty-like bending stiffness term to Eq. (35), thus enabling the application of a rotation-free shell formulation to structures with topology that may not be represented using a single smooth mapping. The additional benefits of the bending strip approach, such as the possibility of coupling solids and shells, are described in [43].

For alternative rotation-free shell formulations the reader is referred to [13, 15, 72–77]

3.3. Time Integration of the FSI Equations and Coupling

The ALE formulation for fluid mechanics and the Lagrangian formulation for the structural mechanics give a natural setting for a finite-difference-in-time time integration of this coupled FSI system. We employ the Generalized-alpha technique [48, 78, 79] in this work, which is a fully-implicit second-order accurate method with control over the dissipation of high-frequency modes. At each time step the combined fluid, structure and mesh motion discrete residuals are converged to zero by means of a block-iterative FSI coupling approach (see [80–82] for the terminology). The block-iterative approach consists of repeating the following sequence of linear solves: 1. We obtain the fluid mechanics solution increment holding the structural and mesh solutions fixed. 2. We update the fluid mechanics solution, compute the fluid traction force on the structure and compute the structural solution increment; 3. We update the structural solution and use elastic mesh motion to update the fluid domain velocity and position. We note that only the deflection part of the mesh motion is computed using linear elastostatics, while the rotation part is computed exactly. This three-step iteration sequence is repeated until convergence to an appropriately coupled discrete solution is achieved.

Remark 10. The block-iterative approach to FSI coupling is stable for our application. This is in part because wind turbine blades are heavy relative to the surrounding air. In addition, the fluid mechanics problem is not posed on an enclosed domain, which presents difficulties for incompressible flow [83]. As a result, FSI coupling for wind turbine problems does not present as significant of a challenge as it does for the applications in, for example, cardiovascular blood flow [47, 49], or parachute modeling [84, 85]. In the latter cases, a quasi-direct FSI coupling approach, which couples the fluid and structural equations in the left-hand-side matrix, appears to be critical for achieving the necessary robustness of the computational procedures. The challenges for wind turbine simulations lie in the ability to accurately approximate the individual fluid and structural mechanics problems at such large spatial scales, and in the management of the fluid mechanics mesh during the simulations.

So far, we discussed weakly enforced boundary conditions for the fluid mechanics problem. In the case strong boundary conditions are employed, we propose to modify the fluid mechanics formulation and the FSI coupling procedures as follows.

- Set $\mathbf{u}_1^h = \hat{\mathbf{u}}^h = \Pi_1^h \mathbf{u}_2^h$ strongly on $(\Gamma_{\mathrm{I}})_t$.

- This reduces the discrete formulation of the fluid mechanics problem given by Eq. (24) to: find $\mathbf{u}_1^h$ and p^h such that for all $(\mathbf{w}_1^h)_0$ and q_1^h

$$B_1^{MS}(\{(\mathbf{w}_1^h)_0, q^h\}, \{\mathbf{u}_1^h, p^h\}) - F_1^{MS}(\{(\mathbf{w}_1^h)_0, q^h\}) = 0,$$

  where the subscript 0 on $\mathbf{w}_1^h$ indicates that a subset of the fluid mechanics test functions, which are not supported on the fluid–structure interface, is employed.

- Given the fluid mechanics solution from the previous step, compute the fluid traction vector on the fluid–structure interface as: find $\mathbf{t}_1^h$, such that for all $(\mathbf{w}_1^h)_g$

$$\int_{(\Gamma_1)_t} (\mathbf{w}_1^h)_g \cdot \mathbf{t}_1^h \, \mathrm{d}\Gamma = B_1^{MS}(\{(\mathbf{w}_1^h)_g, q^h\}, \{\mathbf{u}_1^h, p^h\}) - F_1^{MS}(\{(\mathbf{w}_1^h)_g, q^h\}), \tag{37}$$

  where the subscript g on $\mathbf{w}_1^h$ indicates that a subset of the fluid mechanics test functions, which are supported on the fluid–structure interface, is employed. This is known as the conservative definition of the traction vector on the boundary with strongly enforced essential boundary conditions (see, e.g., [86, 87] for the importance of using conservative flux definitions on essential boundaries and in coupled problems).

- Project the computed fluid mechanics traction vector $\mathbf{t}_1^h$ to the structural mechanics domain discretization of the fluid–structure interface and solve the structural mechanics problem. In the case of matching fluid–structure interface discretization no projection is necessary.

- Update the fluid mechanics mesh position and velocity, check for convergence of the fluid, structure and mesh residuals, and repeat the iteration if necessary. If not, go to the next time step.

3.4. Data Transfer for IGA and FEM Surface Discretizations

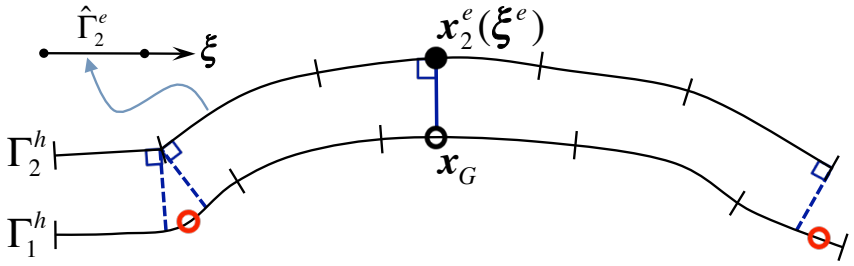

Figure 1: Illustration of the closest point projection, and the associated difficulties, using 2D curves. Vertical notches on the curves denote element boundaries in the physical domain.

Non-matching interface discretizations in the FSI problem necessitate the use of interpolation or projection of kinematic and traction data between the fluid and structural surface meshes (see, e.g., [31, 67], or the developments in the previous section). Here we describe the computational procedures, which can simultaneously handle IGA and FEM discretizations.

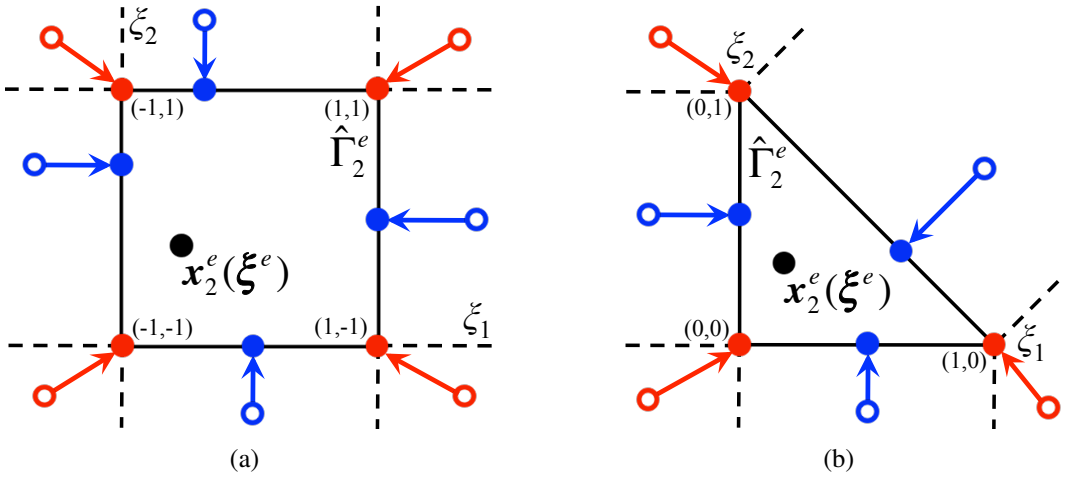

Figure 2: Illustration of the procedure of finding the closest point in the case the Newton-Raphson iteration converges to a parametric value outside an element. In this case, additional candidates for the closest point are searched on element boundaries and corners. The procedure is equally applicable to the case of triangular and rectangular topology of the underlying surface.

Let f_1^h and f_2^h be the arbitrary functions defined on two surfaces Γ_1^h and Γ_2^h, respectively. The functions are represented in the discrete IGA or FEM spaces defined on the surfaces, which may be the standalone surfaces or boundaries of the corresponding volumetric domains. We also define Π_1^h and Π_2^h to be the L^2-projection operators corresponding to the discrete function spaces defined on Γ_1^h and Γ_2^h, respectively. We write

$$f_1^h = \Pi_1^h f_2^h \tag{38}$$

to mean that f_1^h is an L^2-projection of f_2^h onto the space of functions defined on Γ_1^h. In the case Γ_1^h and Γ_2^h coincide geometrically, Eq. (38) is unambiguous. However, when the two domains are mismatched, which is typically the case for FSI involving complex structural surfaces, the L^2-projection given by Eq. (38) requires a more careful consideration.

The matrix form of Eq. (38) may be written as

$$\sum_{B\in\boldsymbol{\eta}_1} \int_{\Gamma_1^h} N_A N_B \,\mathrm{d}\Gamma f_B = \int_{\Gamma_1^h} N_A f_2^h \,\mathrm{d}\Gamma, \tag{39}$$

N_A's are the basis functions defined on Γ_1^h, $\boldsymbol{\eta}_1$ is their set, f_B's are the discrete solution coefficients of the L^2-projection problem giving $f_1^h = \sum_{B\in\boldsymbol{\eta}_1} N_B f_B$, and $A, B \in \boldsymbol{\eta}_1$. The Gauss quadrature (or other numerical integration) approximation of the right-hand-side of Eq. (39) gives

$$\int_{\Gamma_1^h} N_A f_2^h \,\mathrm{d}\Gamma \approx \sum_{e=1}^{N_{el}} \sum_{i=1}^{N_{int}^e} N_A(\boldsymbol{\zeta}_i^e) f_2^h(\boldsymbol{\zeta}_i^e) W_i^e J(\boldsymbol{\zeta}_i^e), \tag{40}$$

where N_{el} is the number of elements on Γ_1^h, N_{int}^e is a number of Gauss points used on element e, $\boldsymbol{\zeta}_i^e$'s are the locations of the Gauss points in the parametric domain of element e, W_i^e's are the corresponding quadrature weights, and J is the surface Jacobian determinant.

In the case of surface discretizations matching geometrically, the quadrature formula given by Eq. (40) may be evaluated directly. In the case of non-matching discretizations, however, "$f_2^h(\boldsymbol{\zeta}_i^e)$" needs to be suitably defined. We do this as follows: for every quadrature point on Γ_1^h we find its *closest point* on Γ_2^h and evaluate f_2^h there. The closest point, illustrated in Figure 1, is defined as follows: if $\mathbf{x}_G$ is a generic point on Γ_1^h, then its closest point $\mathbf{x}_2^e(\boldsymbol{\xi}^e)$ on Γ_2^h is such that the distance $\|\mathbf{x}_2^e(\boldsymbol{\xi}^e) - \mathbf{x}_G\|$ is minimized. Here $\mathbf{x}_2^e(\boldsymbol{\xi}^e)$ is the geometrical mapping defined on a parametric element $\hat{\Gamma}_2^e$ of the surface Γ_2^h, and $\boldsymbol{\xi}^e$ are the parametric coordinates of this element. The closest point is characterized by the solution of the following problem: find $\hat{\Gamma}_2^e$ and $\boldsymbol{\xi}^e = \{\xi_1^e, \xi_2^e\}^T \in \hat{\Gamma}_2^e$ such that

$$\frac{\partial \mathbf{x}_2^e(\boldsymbol{\xi}^e)}{\partial \xi_1^e} \cdot (\mathbf{x}_2^e(\boldsymbol{\xi}^e) - \mathbf{x}_G) = 0 \tag{41}$$

$$\frac{\partial \mathbf{x}_2^e(\boldsymbol{\xi}^e)}{\partial \xi_2^e} \cdot (\mathbf{x}_2^e(\boldsymbol{\xi}^e) - \mathbf{x}_G) = 0, \tag{42}$$

that is, the distance vector $(\mathbf{x}_2^e(\boldsymbol{\xi}^e) - \mathbf{x}_G)$ is orthogonal to the two tangent vectors $\frac{\partial \mathbf{x}_2^e(\boldsymbol{\xi}^e)}{\partial \xi_1^e}$ and $\frac{\partial \mathbf{x}_2^e(\boldsymbol{\xi}^e)}{\partial \xi_2^e}$ of the surface Γ_2^h. The 2×2 system of equations (41)–(42) is solved using the Newton-Raphson iteration procedure. We find that a complete linearization of the equations is important for rapid convergence of the iterations.

Remark 11. Note that the problem of finding the closest point and using it to define a projection between two possibly non-matching surfaces is form-identical in IGA and FEM. All that is needed is a parameterized surface, the notion of a parametric element, and the ability to define a set of linearly independent basis functions on the surface. These features are common to both IGA and FEM.

Existence (and uniqueness) of closest points depends on several factors. Situations that may lead to non-existence of solutions in the sense of Eqs. (41)–(42) typically arise in the case of non-smooth surfaces with discontinuous tangent vectors, or in the case of surfaces that are not properly aligned (see Figure 1 for an illustration). As a result, the procedure described above needs to be augmented to account for these situations. In what follows, we describe an approach that appears to be robust in identifying closest points for arbitrary shaped surfaces.

We assume that for a given $\mathbf{x}_G$ we solved the nonlinear system given by Eqs. (41)–(42) for $\{\xi_1^e, \xi_2^e\}^T$ on every element $\hat{\Gamma}_2^e$. We also assume that $\hat{\Gamma}_2^e$ is either a bi-unit quad or an isosceles right triangle (see Figure 2). In the case of rectangular topology, for an appropriate subset of elements in Γ_2^h, we go through the following cases:

1. If $|\xi_1^e| \leq 1$ and $|\xi_2^e| \leq 1$, store ξ_1^e and ξ_2^e.
2. If $|\xi_1^e| > 1$ and $|\xi_2^e| \leq 1$,

$$\text{set } \xi_1^e = \operatorname{sgn}(\xi_1^e), \text{ then solve } \frac{\partial \mathbf{x}_2^e(\boldsymbol{\xi}^e)}{\partial \xi_2^e} \cdot (\mathbf{x}_2^e(\boldsymbol{\xi}^e) - \mathbf{x}_G) = 0. \tag{43}$$

3. If $|\xi_1^e| \leq 1$ and $|\xi_2^e| > 1$,

$$\text{set } \xi_2^e = \text{sgn}(\xi_2^e), \text{ then solve } \frac{\partial \mathbf{x}_2^e(\boldsymbol{\xi}^e)}{\partial \xi_1^e} \cdot (\mathbf{x}_2^e(\boldsymbol{\xi}^e) - \mathbf{x}_G) = 0. \tag{44}$$

4. If $|\xi_1^e| > 1$ and $|\xi_2^e| > 1$, or if the above case 2 or 3 generates a parameter that is out of bounds,

$$\text{set } \xi_1^e = \text{sgn}(\xi_1^e), \text{ and set } \xi_2^e = \text{sgn}(\xi_2^e) \tag{45}$$

At this point each element in the subset generates one candidate for the closest point, and we select the candidate that minimizes $||(\mathbf{x}_2^e(\boldsymbol{\xi}^e) - \mathbf{x}_G)||$. The four cases described above are illustrated in Figure 2a. The triangular topology case, shown in Figure 2b is handled in an analogous fashion. The rectangular topology approach is suitable for NURBS, T-spline, Catmull-Clark subdivision, and quadrilateral FEM surfaces, while the triangular topology approach may be used for Loop subdivison and triangular FEM surfaces.

4. Computational results

4.1. Testing of the Data Transfer Algorithm

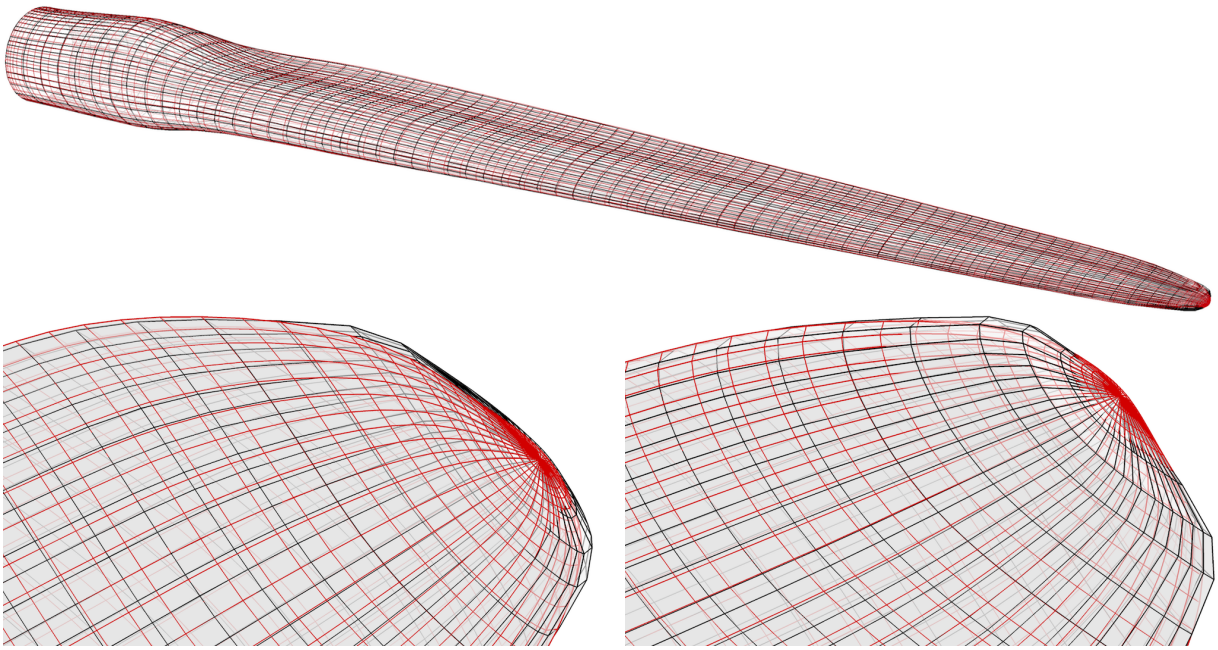

Figure 3: Surface meshes of the wind turbine blade used in the computations in this paper. The black mesh lines correspond to a bi-cubic T-spline discretization and the red mesh lines correspond to a bi-quadratic NURBS discretization. Top: complete blade surface. Bottom: zoom on the blade tip, where the differences between the two surfaces are clearly visible.

Before presenting the FSI results, we test the performance of the data transfer algorithm. For this, a 5MW wind turbine rotor, assumed rigid, is simulated at prescribed steady inlet wind

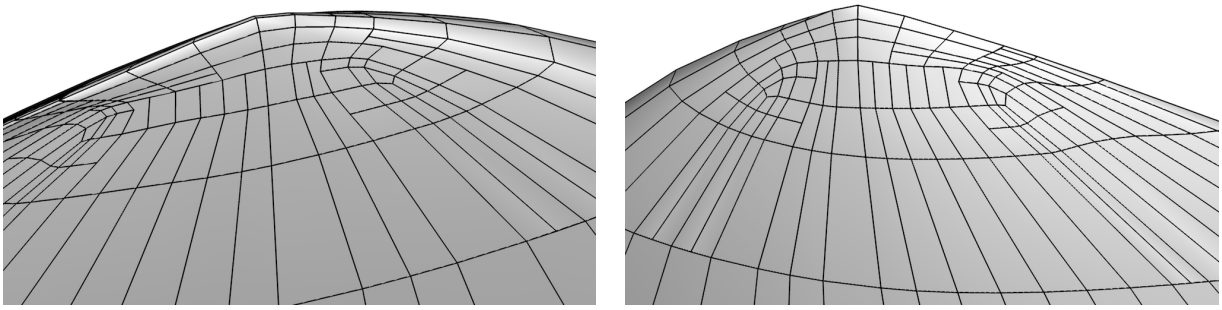

(a) (b)

Figure 4: Zoom on the tip of the blade surface mesh reparameterized by T-splines. Note that the tip singularity is removed. Several extraordinary points [3, 88] are used to model the geometry in the vicinity of the tip. (a) Pressure side. (b) Suction side.

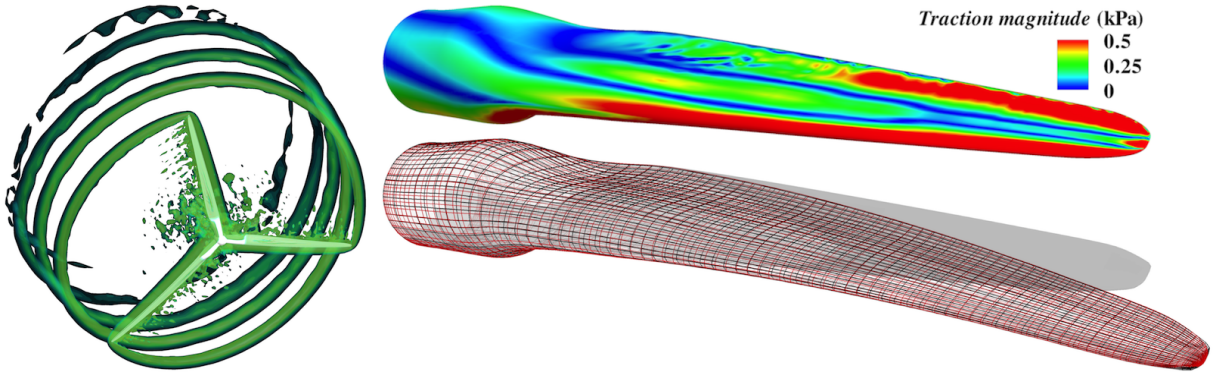

Figure 5: Left: Aerodynamics of the rigidly rotating wind turbine rotor. Isosurfaces of wind speed at a time instant. Top right: Magnitude of the aerodynamic traction vector on the blade surface. Bottom right: The blade in the reference and deformed configurations. NURBS and T-spline meshes are superposed on the deformed configuration, showing no visible differences between the two structural mechanics solutions.

velocity of 11.4 m/s and rotor angular velocity of 12.1 rpm. This setup corresponds to one of the cases reported in [33]. The dimensions of the problem domain, the NURBS mesh employed, and the overall problem setup are the same as in [32, 35]. The aerodynamic traction vector is collected on the NURBS surface of the rotor, and used in the structural computations of a single wind turbine blade whose surface meshes are shown in Figure 3. Here we employ two discretizations of the blade. One is based on quadratic NURBS and the other on cubic T-splines. The T-spline surface was obtained by reparameterizing the NURBS surface. Singularity in the NURBS geometrical mapping due to coalesced control points at the blade tip is removed during the reparameterization process (see Figure 4). Instead, several extraordinary points [3, 88] are used to model the geometry in the vicinity of the tip. The T-spline reparameterization introduced only very minor changes in the blade geometry (e.g., the blade surface area was reduced by about 0.5%). The geometry error may be minimized further by locally adjusting the positions of the T-spline mesh control points.

The NURBS model of the blade, which makes use of the Kirchhoff–Love rotation-free

composite shell formulation, in conjunction with the bending strip method, is described in detail in [32]. There are 4,897 control points in the NURBS mesh. The T-spline model is based on the same structural mechanics formulation, however, no bending strips are employed. The underlying T-spline basis functions have sufficient continuity almost everywhere on the blade surface to obviate the use of bending strips. The T-spline mesh has 3,572 control points.

We compute the blade static response under the action of the fluid traction vector. We also include the effect of the centripetal force due to rotation, which is significant. In the case of the NURBS blade, due to the fact that the fluid and structural meshes are matching at the interface, no data transfer is necessary. The predicted blade tip deflection is 3.6098 m. We repeat the calculation for the T-spline blade. The T-spline implementation in the isogeometric Kirchhoff–Love shell code makes use of the Bézier extraction decomposition of the analysis geometry (see [16, 17]). In this case, we project the aerodynamic traction vector from the boundary of the fluid mechanics NURBS mesh to the T-spline structural mesh, compute the structural displacement taking the centripetal force into account, and project the displacement back to the NURBS mesh. In this case, the tip deflection is predicted to be 3.6193 m. This gives the relative error of 0.26% between the matching and non-matching discretization simulations, which is felt to be almost negligible. We also assessed the accuracy of the load transfer by comparing the global aerodynamic force and moment on the NURBS and T-spline meshes. After the load transfer, the error in the global force is only 0.14%, and the error in the global moment is only 0.10%.

The results of the aerodynamics and two structural computations are shown in Figure 5.

4.2. FSI Simulations

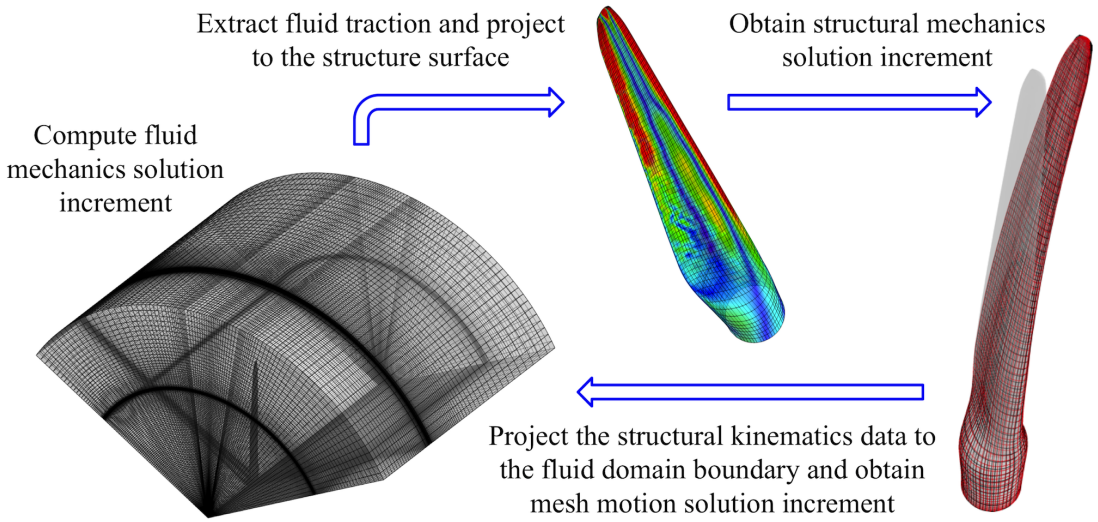

Figure 6: Illustration of the block-iterative FSI methodology for the simulation of wind turbine rotors. Due to the relatively heavy weight of the wind turbine blades with respect to the surrounding air, this type of coupling is sufficient for rapid convergence of the coupled nonlinear FSI equation system.

In this section we present FSI simulations of the 5MW wind turbine rotor. We first show the case where we couple the NURBS fluid mechanics and T-spline structural mechanics discretiza-

tions. We then show the results of the coupling between low-order FEM for fluid mechanics and T-splines for structural mechanics. The FSI coupling procedure employed in both cases is described in Section 3 and is also illustrated in Figure 6. The strong boundary condition version of the FSI formulation is employed in the case of NURBS and T-spline coupling. This is due to the fact that the NURBS fluid mechanics mesh has sufficient boundary layer refinement to produce accurate results for the quantities of interest in the simulation. In the case of FEM and T-spline coupling, because of the lack of adequate boundary layer resolution, a weakly enforced boundary condition version of the FSI coupling method is employed. In both cases we use steady inlet wind velocity of 11.4 m/s and rotor angular velocity of 12.1 rpm, and compare the results with the NURBS matching-interface computation, which we take as a benchmark calculation.

4.2.1. Coupling of NURBS for Fluid and T-Splines for Structural Mechanics

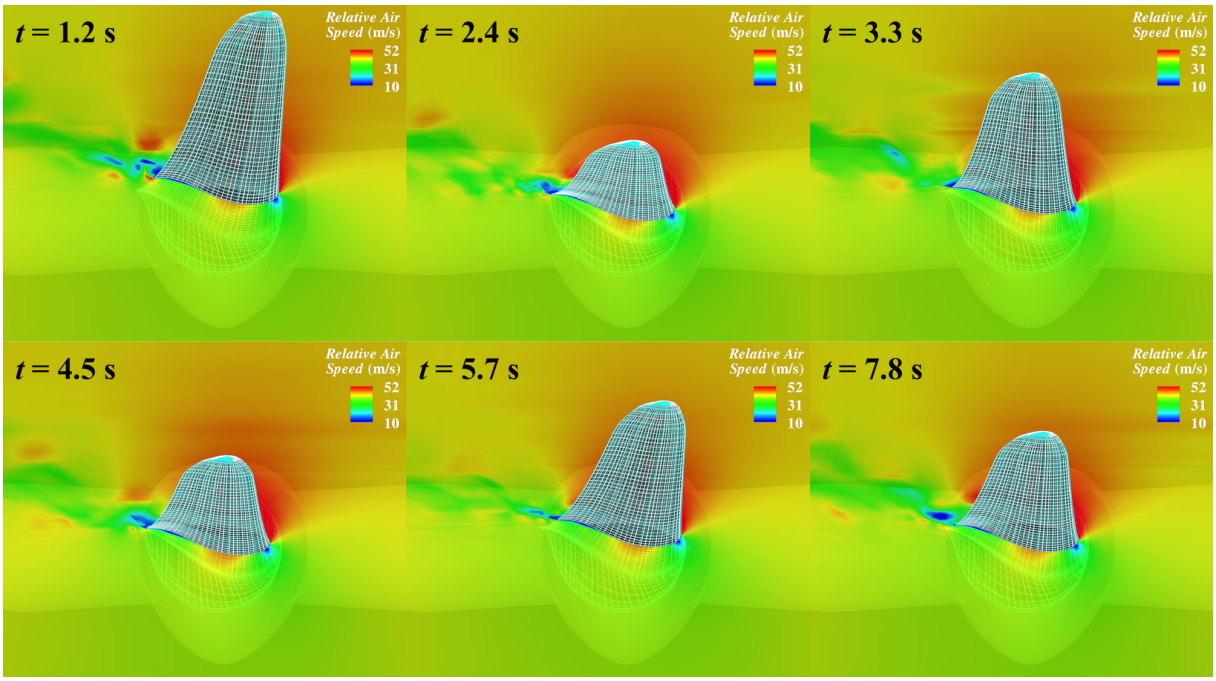

Figure 7: Relative air speed in a blade cross-section, rotated to the reference configuration, corresponding to a 30 m radial cut. Note that the blade deflection is quite significant. Both the NURBS mesh of the fluid domain boundary and the T-spline mesh of the blade are shown on the blade surface.

We perform an FSI computation for 8 s of real time, by which time the initial transient nearly settles. For the three-bladed 5MW rotor we perform a single-blade simulation with only one third of the cylindrical computational domain and rotationally-periodic boundary conditions. Snapshots of the relative air speed on the blade axis cross-section at different times during the simulation are shown in Figures 7 and 8. The results are shown on the deformed configuration, which is rotated back to the initial position in order to show the blade deflection. Both the T-spline mesh of the blade and the NURBS mesh of the fluid mechanics domain boundary corresponding to the fluid–structure interface are superposed on the figures. It is clear, especially

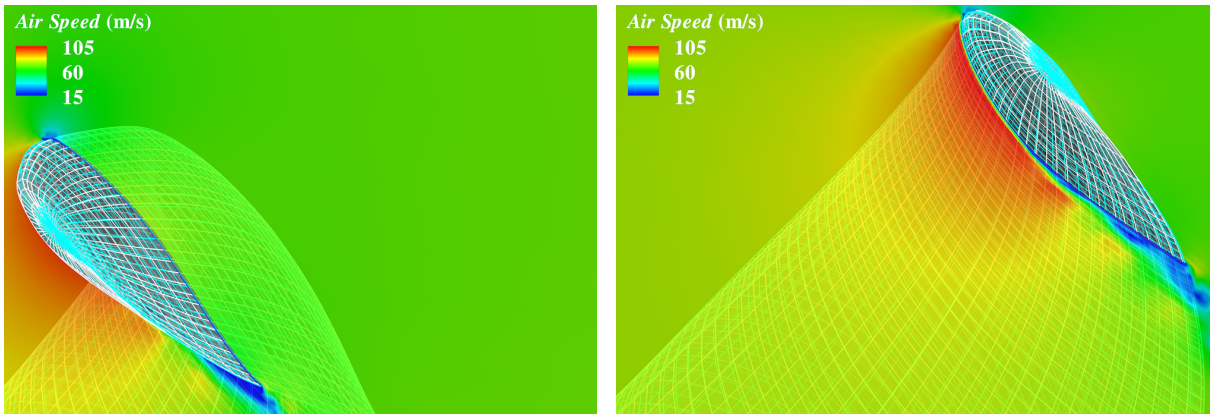

(a) (b)

Figure 8: Relative air speed in a blade cross-section, rotated to the reference configuration. Zoom on the blade tip, showing the superposition of the NURBS mesh of the fluid domain boundary and the T-spline mesh of the blade. The snapshots correspond to the time close to (a) the beginning and (b) the end of the simulation, illustrating that the T-spline and NURBS meshes stay "glued" to one another for the entire duration of the simulation.

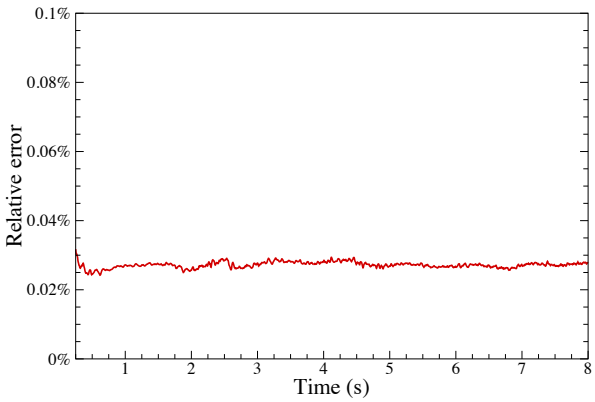

Figure 9: Relative error between the T-spline mesh tip displacement and the L^2-projection thereof on the surface mesh of the fluid domain. The relative error is very small and stays nearly constant for the entire simulation. This shows the that structural kinematics is correctly and accurately transferred to the fluid mesh.

from Figure 8, which zooms on the blade tip and shows how different the NURBS and T-spline meshes are, that the meshes stay "glued" to one another for the entire simulation. In Figure 9 we plot the blade tip displacement error between the fluid and structural surface meshes as a function of time. The sole source of the error is the L^2-projection of the kinematic data between the two non-matching meshes. We note that the error magnitude does not exceed 0.03%.

The remainder of this section compares the non-matching mesh simulation with the T-spline structural model of the blade, and the all-NURBS (fluid and structure) simulation using a *matching discretization* of the fluid–structure interface. Figure 10 shows the time history of flapwise and edgewise tip displacement. For this quantity, the results of the matching and non-matching mesh simulations are nearly indistinguishable for the entire duration of the simulation. Time history of the aerodynamic torque is shown in Figure 11. Both simulations produce the same

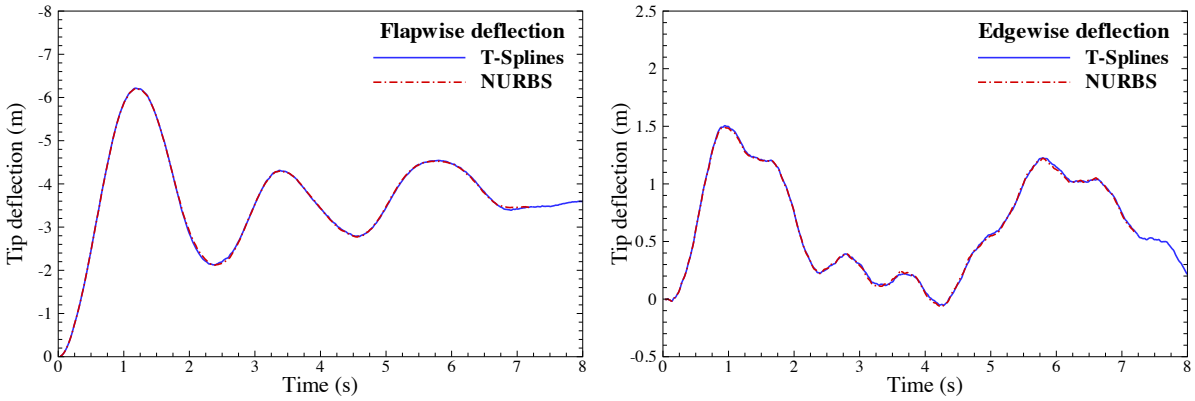

Figure 10: Time history of the blade tip displacement. Comparison between the matching and non-matching interface discretization FSI simulations reveals virtually no difference in tip displacement.

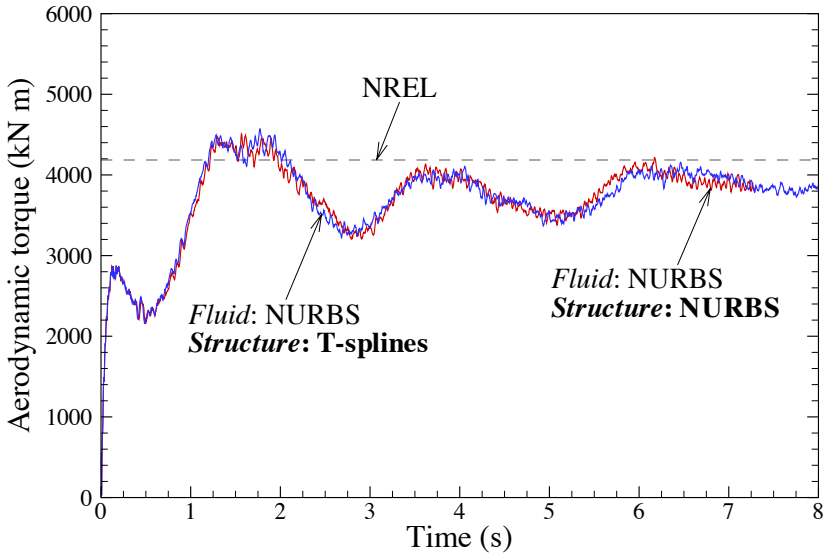

Figure 11: Time history of the aerodynamic torque. Comparison between the matching and non-matching interface discretization FSI simulations reveals no difference in large-scale response, while minor differences are present in the small-scale oscillations. Both simulations compare favorably to the NREL data [33].

large-scale response, with some differences in the details of the low-amplitude high-frequency torque oscillations. The results compare favorably to the aerodynamic torque data reported by NREL in [33] for this blade design under the same wind and rotor speed conditions. The time history of the twist angle at two different blade axial locations is shown in Figure 12. The blade twists and untwists as it undergoes rotational motion. This is due to the reversal of the gravity vector with respect to the aerodynamic traction vector as the blade tip passes its low and high points. High-frequency twisting oscillations are present, showing minor differences between the two simulations, however, the agreement between the matching and non-matching FSI cases is very good.

This example shows that the proposed coupling methodology is such that there is very little

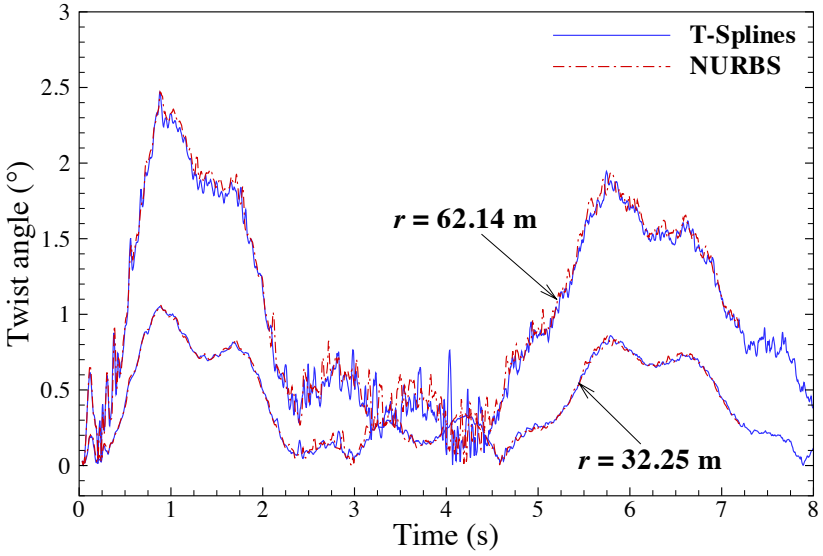

Figure 12: Time history of the twist angle at the two cross-sections on the blade axis. Comparison between the matching and non-matching interface discretization FSI simulations reveals no difference in large-scale response, while minor differences are present in the small-scale oscillations.

or virtually no accuracy loss due to the presence of the non-matching FSI interface discretization.

4.2.2. Coupling of FEM for Fluid and T-Splines for Structural Mechanics

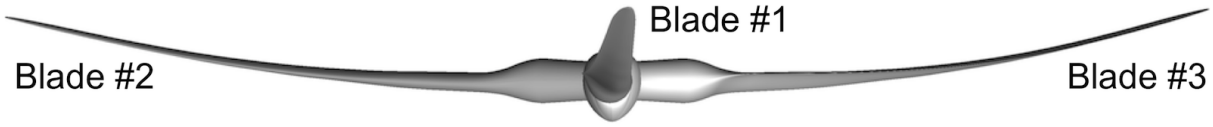

Figure 13: Three-bladed rotor in a deformed configuration at a time instant during the FSI simulation.

In this section, we show preliminary computational results for the FSI coupling of FEM and IGA. Instead of using rotational periodicity, we compute the full domain with three rotor blades. We use an automatic mesh generator to create a linear tetrahedral mesh of the aerodynamics domain, consisting of only 1,193,404 nodes. This is a significantly coarser fluid mechanics mesh than the NURBS mesh used in the previous section. About 1.5 million control points were employed for the discretization of 1/3 of the fluid domain in the case of the quadratics NURBS mesh. The same structural T-spline mesh is employed here as in the previous section.

Figure 13 shows the three-bladed rotor at one time instant during the FSI simulation. Note that some differences in the flap-wise deflection are present from one blade to another. Figure 14 shows the time history of the aerodynamic torque and the flapwise deflection of the rotor blades. These quantities are reported for each blade individually, and the results are compared with a NURBS/T-spline simulation from the previous section. While there is a very reasonable overall agreement, the FEM/T-spline simulation predicts larger peak-to-peak variations in both quantities during the initial transient response of the coupled system.

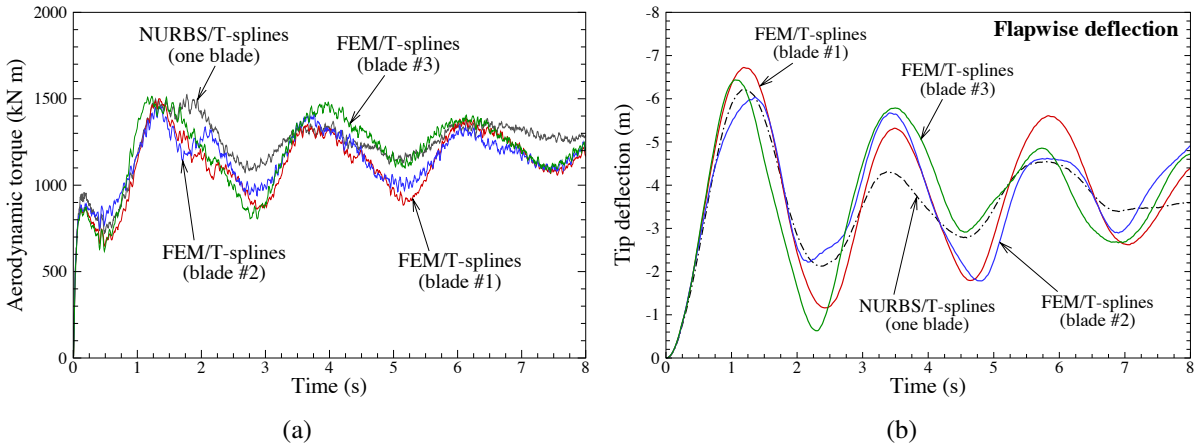

Figure 14: Time history of the (a) aerodynamic torque and (b) flapwise deflection. Comparison between the FEM/T-spline and NURBS/T-spline FSI simulations. The data is presented for each blade individually in the case of FEM/T-spline simulation. The numbering of the blades is consistent with that in Figure 13.

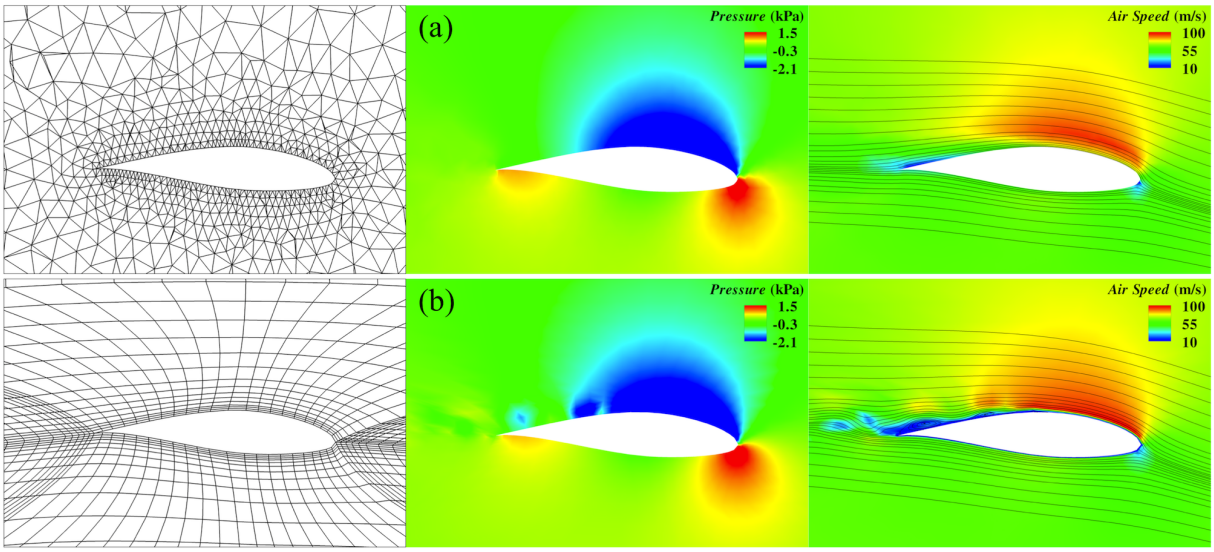

Figure 15: Comparison of aerodynamic results between (a) FEM/T-spline, and (b) NURBS/T-spline FSI simulations. Mesh (left), pressure (middle), and relative air speed (right) at a fixed time $t = 7.5$ s plotted on a cross-section corresponding to 80% of the blade radius.

Some of the discrepancies in the results come from the differences in the starting configuration for each blade, which directly affects the structural dynamics of the rotor. Other differences come from the prediction of the aerodynamics phenomena. Figure 15 compares relative air speed and pressure distribution at a fixed time on a cross-section corresponding to 80% of the blade radius. We notice that the significantly finer NURBS mesh is capable of resolving some of the trailing edge turbulence, while the coarse FEM mesh produces a "smoother" solution. Nevertheless, despite the large differences in mesh resolution and the lack of real boundary-layer meshing in the case of linear FEM, the large-scale features of the flow are qualitatively

and quantitatively very similar for both discretizations.

5. Conclusions

Although non-matching grids have been used in FSI for many years, we feel the proposed framework and formulations are novel. The augmented Lagrangian framework with a formal elimination of the Lagrange multiplier generates a family of FSI formulations at the continuum level, which serves as a point of departure for the discrete FSI formulation proposed in this work. The augmented Lagrangian approach naturally motivates weak enforcement of essential boundary conditions for the fluid mechanics problem, explains the structure of the penalty terms that stabilize the formulation, and leads to the definition of the fluid traction vector acting on the structural surface that consistently accounts for slip velocity.

We proposed a robust procedure for transferring kinetic and traction data between the non-matching IGA and FEM discretizations.

We successfully applied the proposed framework to the simulation of a 5MW wind turbine rotor at full scale. The computational results suggest that virtually no accuracy is lost due to the use of non-matching discretizations. Preliminary simulations coupling low-order FEM for the fluid and IGA for the structure are likewise fairly successful.

In the future work we plan to perform more extensive testing of FEM and IGA coupling. We plan to include rotor-tower interaction in these and other computations.

Acknowledgement

We thank the Texas Advanced Computing Center (TACC) at the University of Texas at Austin for providing HPC resources that have contributed to the research results reported within this paper. M.-C. Hsu was partially supported by the Los Alamos–UC San Diego Educational Collaboration Fellowship. Y. Bazilevs would like to acknowledge the support of the NSF CAREER Award No. 1055091 and the Air Force Office of Scientific Research Award FA9550-12-1-0005. M.A. Scott was partially supported by an CAM Graduate Fellowship at the Institute for Computational Engineering and Sciences (ICES), the University of Texas at Austin.

References

[1] T.J.R. Hughes, J.A. Cottrell, and Y. Bazilevs. Isogeometric analysis: CAD, finite elements, NURBS, exact geometry and mesh refinement. *Computer Methods in Applied Mechanics and Engineering*, 194:4135–4195, 2005.

[2] J.A. Cottrell, T.J.R. Hughes, and Y. Bazilevs. *Isogeometric Analysis: Toward Integration of CAD and FEA*. Wiley, Chichester, 2009.

[3] T.W. Sederberg, J. Zheng, A. Bakenov, and A. Nasri. T-splines and T-NURCCS. *ACM Transactions on Graphics*, 22(3):477–484, 2003.

[4] T. W. Sederberg, D.L. Cardon, G.T. Finnigan, N.S. North, J. Zheng, and T. Lyche. T-spline simplification and local refinement. *ACM Transactions on Graphics*, 23(3):276–283, 2004.

[5] Y. Bazilevs, V.M. Calo, J.A. Cottrell, J.A. Evans, T.J.R. Hughes, S. Lipton, M.A. Scott, and T.W. Sederberg. Isogeometric analysis using T-splines. *Computer Methods in Applied Mechanics and Engineering*, 199:229–263, 2010.

[6] M.R. Dörfel, B. Jüttler, and B. Simeon. Adaptive isogeometric analysis by local *h*-refinement with T-splines. *Computer Methods in Applied Mechanics and Engineering*, 199:264–275, 2010.

[7] C.V. Verhoosel, M.A. Scott, T.J.R. Hughes, and R. de Borst. An isogeometric analysis approach to gradient damage models. *International Journal for Numerical Methods in Engineering*, 86:115–134, 2011.

[8] M.J Borden, M.A. Scott, C.V. Verhoosel, T.J.R. Hughes, and C.M. Landis. A phase-field description of dynamic brittle fracture. *Computer Methods in Applied Mechanics and Engineering*, 217–220:77–95, 2012.

[9] M.A. Scott, X. Li, T.W. Sederberg, and T.J.R. Hughes. Local refinement of analysis-suitable T-splines. *Computer Methods in Applied Mechanics and Engineering*, 213–216:206–222, 2012.

[10] X. Li, J. Zheng, T.W. Sederberg, T.J.R. Hughes, and M. A. Scott. On linear independence of T-spline blending functions. *Computer-Aided Geometric Design*, 29:63–76, 2012.

[11] E. Cohen, T. Martin, R.M. Kirby, T. Lyche, and R.F. Riesenfeld. Analysis-aware modeling: Understanding quality considerations in modeling for isogeometric analysis. *Computer Methods in Applied Mechanics and Engineering*, 199:334–356, 2010.

[12] W. Wang and Y. Zhang. Wavelets-based NURBS simplification and fairing. *Computer Methods in Applied Mechanics and Engineering*, 199:290–300, 2010.

[13] D.J. Benson, Y. Bazilevs, M.C. Hsu, and T.J.R. Hughes. Isogeometric shell analysis: The Reissner–Mindlin shell. *Computer Methods in Applied Mechanics and Engineering*, 199:276–289, 2010.

[14] D.J. Benson, Y. Bazilevs, E. De Luycker, M.-C. Hsu, M. Scott, T.J.R. Hughes, and T. Belytschko. A generalized finite element formulation for arbitrary basis functions: from isogeometric analysis to XFEM. *International Journal for Numerical Methods in Engineering*, 83:765–785, 2010.

[15] D.J. Benson, Y. Bazilevs, M.C. Hsu, and T.J.R. Hughes. A large deformation, rotation-free, isogeometric shell. *Computer Methods in Applied Mechanics and Engineering*, 200:1367–1378, 2011.

[16] M.J. Borden, M.A. Scott, J.A. Evans, and T.J.R. Hughes. Isogeometric finite element data structures based on Bézier extraction of NURBS. *International Journal for Numerical Methods in Engineering*, 87:15–47, 2011.

[17] M.A. Scott, M.J. Borden, C.V. Verhoosel, T.W. Sederberg, and T.J.R. Hughes. Isogeometric finite element data structures based on Bézier extraction of T-splines. *International Journal for Numerical Methods in Engineering*, 88:126–156, 2011.

[18] T. Elguedj, Y. Bazilevs, V.M. Calo, and T.J.R. Hughes. $\overline{\mathrm{B}}$ and $\overline{\mathrm{F}}$ projection methods for nearly incompressible linear and non-linear elasticity and plasticity using higher-order NURBS elements. *Computer Methods in Applied Mechanics and Engineering*, 197:2732–2762, 2008.

[19] H. Gomez, V.M. Calo, Y. Bazilevs, and T.J.R. Hughes. Isogeometric analysis of the Cahn–Hilliard phase-field model. *Computer Methods in Applied Mechanics and Engineering*, 197:4333–4352, 2008.

[20] H. Gomez, T.J.R. Hughes, X. Nogueira, and V.M. Calo. Isogeometric analysis of the isothermal Navier–Stokes–Korteweg equations. *Computer Methods in Applied Mechanics and Engineering*, 199:1828–1840, 2010.

[21] Y. Zhang, Y. Bazilevs, S. Goswami, C. Bajaj, and T.J.R. Hughes. Patient-specific vascular NURBS modeling for isogeometric analysis of blood flow. *Computer Methods in Applied Mechanics and Engineering*, 196:2943–2959, 2007.

[22] Y. Bazilevs, M.-C. Hsu, I. Akkerman, S. Wright, K. Takizawa, B. Henicke, T. Spielman, and T.E. Tezduyar. 3D simulation of wind turbine rotors at full scale. Part I: Geometry modeling and aerodynamics. *International Journal for Numerical Methods in Fluids*, 65:207–235, 2011.

[23] W. Wang, Y. Zhang, M.A. Scott, and T.J.R. Hughes. Converting an unstructured quadrilateral mesh to a standard T-spline surface. *Computational Mechanics*, 48:477–498, 2011.

[24] W. Wang, Y. Zhang, M.A. Scott, and T.J.R. Hughes. Converting an unstructured quadrilateral/hexahedral mesh to a rational T-spline. *Computational Mechanics*, 2012. DOI: 10.1007/s00466-011-0674-6.

[25] J.A. Cottrell, A. Reali, Y. Bazilevs, and T.J.R. Hughes. Isogeometric analysis of structural vibrations. *Computer Methods in Applied Mechanics and Engineering*, 195:5257–5297, 2006.

[26] F. Auricchio, L. Beirão da Veiga, C. Lovadina, and A. Reali. The importance of the exact satisfaction of the incompressibility constraint in nonlinear elasticity: Mixed FEMs versus NURBS-based approximations. *Computer Methods in Applied Mechanics and Engineering*, 199:314–323, 2010.

[27] I. Akkerman, Y. Bazilevs, V.M. Calo, T.J.R. Hughes, and S. Hulshoff. The role of continuity in residual-based variational multiscale modeling of turbulence. *Computational Mechanics*, 41:371–378, 2008.

[28] K. Takizawa, B. Henicke, T.E. Tezduyar, M.-C. Hsu, and Y. Bazilevs. Stabilized space-time computation of wind-turbine rotor aerodynamics. *Computational Mechanics*, 48:333–344, 2011.

[29] K. Takizawa, B. Henicke, D. Montes, T.E. Tezduyar, M.-C. Hsu, and Y. Bazilevs. Numerical-performance studies for the stabilized space-time computation of wind-turbine rotor aerodynamics. *Computational Mechanics*, 48:647–657, 2011.

[30] M.-C. Hsu, I. Akkerman, and Y. Bazilevs. Wind turbine aerodynamics using ALE–VMS: Validation and the role of weakly enforced boundary conditions. *Computational Mechanics*, 2012. Published online. DOI: 10.1007/s00466-012-0686-x.

[31] C. Farhat, M. Lesoinne, and P. Le Tallec. Load and motion transfer algorithms for fluid/structure interaction problems with non-matching discrete interfaces: Momentum and energy conservation, optimal discretization and application to aeroelasticity. *Computer Methods in Applied Mechanics and Engineering*, 157:95–114, 1998.

[32] Y. Bazilevs, M.-C. Hsu, J. Kiendl, R. Wüchner, and K.-U. Bletzinger. 3D simulation of wind turbine rotors at full scale. Part II: Fluid–structure interaction modeling with composite blades. *International Journal for Numerical Methods in Fluids*, 65:236–253, 2011.

[33] J. Jonkman, S. Butterfield, W. Musial, and G. Scott. Definition of a 5-MW reference wind turbine for offshore system development. Technical Report NREL/TP-500-38060, National Renewable Energy Laboratory, Golden, CO, 2009.

[34] M.-C. Hsu, I. Akkerman, and Y. Bazilevs. High-performance computing of wind turbine aerodynamics using isogeometric analysis. *Computers & Fluids*, 49:93–100, 2011.

[35] Y. Bazilevs, M.-C. Hsu, J. Kiendl, and D.J. Benson. A computational procedure for prebending of wind turbine blades. *International Journal for Numerical Methods in Engineering*, 89:323–336, 2012.

[36] M.M. Hand, D.A. Simms, L.J. Fingersh, D.W. Jager, J.R. Cotrell, S. Schreck, and S.M. Larwood. Unsteady aerodynamics experiment phase VI: Wind tunnel test configurations and available data campaigns. Technical Report NREL/TP-500-29955, National Renewable Energy Laboratory, Golden, CO, 2001.

[37] Y. Bazilevs, V.M. Calo, J.A. Cottrel, T.J.R. Hughes, A. Reali, and G. Scovazzi. Variational multiscale residual-based turbulence modeling for large eddy simulation of incompressible flows. *Computer Methods in Applied Mechanics and Engineering*, 197:173–201, 2007.

[38] Y. Bazilevs and T.J.R. Hughes. Weak imposition of Dirichlet boundary conditions in fluid mechanics. *Computers & Fluids*, 36:12–26, 2007.

[39] Y. Bazilevs, C. Michler, V.M. Calo, and T.J.R. Hughes. Weak Dirichlet boundary conditions for wall-bounded turbulent flows. *Computer Methods in Applied Mechanics and Engineering*, 196:4853–4862, 2007.

[40] Y. Bazilevs, C. Michler, V.M. Calo, and T.J.R. Hughes. Isogeometric variational multiscale modeling of wall-bounded turbulent flows with weakly enforced boundary conditions on unstretched meshes. *Computer Methods in Applied Mechanics and Engineering*, 199:780–790, 2010.

[41] Y. Bazilevs and I. Akkerman. Large eddy simulation of turbulent Taylor–Couette flow using isogeometric analysis and the residual–based variational multiscale method. *Journal of Computational Physics*, 229:3402–3414, 2010.

[42] J. Kiendl, K.-U. Bletzinger, J. Linhard, and R. Wüchner. Isogeometric shell analysis with Kirchhoff–Love elements. *Computer Methods in Applied Mechanics and Engineering*, 198:3902–3914, 2009.

[43] J. Kiendl, Y. Bazilevs, M.-C. Hsu, R. Wüchner, and K.-U. Bletzinger. The bending strip method for isogeometric analysis of Kirchhoff–Love shell structures comprised of multiple patches. *Computer Methods in Applied Mechanics and Engineering*, 199:2403–2416, 2010.

[44] D.N. Arnold, F. Brezzi, B. Cockburn, and L.D. Marini. Unified analysis of Discontinuous Galerkin methods for elliptic problems. *SIAM Journal of Numerical Analysis*, 39:1749–1779, 2002.

[45] J. Nitsche. Uber ein variationsprinzip zur losung von Dirichlet-problemen bei verwendung von teilraumen, die keinen randbedingungen unterworfen sind. *Abh. Math. Univ. Hamburg*, 36:9–15, 1971.

[46] P. Hansbo and J. Hermansson. Nitsche's method for coupling non-matching meshes in fluid-structure vibrational problems. *Computational Mechanics*, 32:134–139, 2004.

[47] Y. Bazilevs, V.M. Calo, Y. Zhang, and T.J.R. Hughes. Isogeometric fluid-structure interaction analysis with applications to arterial blood flow. *Computational Mechanics*, 38:310–322, 2006.

[48] Y. Bazilevs, V.M. Calo, T.J.R. Hughes, and Y. Zhang. Isogeometric fluid–structure interaction: theory, algorithms, and computations. *Computational Mechanics*, 43:3–37, 2008.

[49] Y. Bazilevs, J.R. Gohean, T.J.R. Hughes, R.D. Moser, and Y. Zhang. Patient-specific isogeometric fluid-structure interaction analysis of thoracic aortic blood flow due to implantation of the Jarvik 2000 left ventricular assist device. *Computer Methods in Applied Mechanics and Engineering*, 198:3534–3550, 2009.

[50] Y. Bazilevs, M.-C. Hsu, D. Benson, S. Sankaran, and A. Marsden. Computational fluid–structure interaction: Methods and application to a total cavopulmonary connection. *Computational Mechanics*, 45:77–89, 2009.

[51] Y. Bazilevs, M.-C. Hsu, Y. Zhang, W. Wang, X. Liang, T. Kvamsdal, R. Brekken, and J. Isaksen. A fully-coupled fluid–structure interaction simulation of cerebral aneurysms. *Computational Mechanics*, 46:3–16, 2010.

[52] Y. Bazilevs, M.-C. Hsu, Y. Zhang, W. Wang, T. Kvamsdal, S. Hentschel, and J. Isaksen. Computational fluid–structure interaction: Methods and application to cerebral aneurysms. *Biomechanics and Modeling in Mechanobiology*, 9:481–498, 2010.

[53] A.N. Brooks and T.J.R. Hughes. Streamline upwind/Petrov–Galerkin formulations for convection dominated flows with particular emphasis on the incompressible Navier–Stokes equations. *Computer Methods in Applied Mechanics and Engineering*, 32:199–259, 1982.

[54] T.J.R. Hughes and T.E. Tezduyar. Finite element methods for first-order hyperbolic systems with particular emphasis on the compressible Euler equations. *Computer Methods in Applied Mechanics and Engineering*, 45:217–284, 1984.

[55] T.E. Tezduyar and Y.J. Park. Discontinuity capturing finite element formulations for nonlinear convection-diffusion-reaction equations. *Computer Methods in Applied Mechanics and Engineering*, 59:307–325, 1986.

[56] T.J.R. Hughes, L.P. Franca, and M. Balestra. A new finite element formulation for computational fluid dynamics: V. Circumventing the Babuška–Brezzi condition: A stable Petrov–Galerkin formulation of the Stokes problem accommodating equal-order interpolations. *Computer Methods in Applied Mechanics and Engineering*, 59:85–99, 1986.

[57] T.E. Tezduyar and Y. Osawa. Finite element stabilization parameters computed from element matrices and vectors. *Computer Methods in Applied Mechanics and Engineering*, 190:411–430, 2000.

[58] T.E. Tezduyar. Computation of moving boundaries and interfaces and stabilization parameters. *International Journal for Numerical Methods in Fluids*, 43:555–575, 2003.

[59] T.J.R. Hughes, G. Scovazzi, and L.P. Franca. Multiscale and stabilized methods. In E. Stein, R. de Borst, and T.J.R. Hughes, editors, *Encyclopedia of Computational Mechanics, Vol. 3, Fluids*, chapter 2. Wiley, 2004.

[60] M.-C. Hsu, Y. Bazilevs, V. M. Calo, T. E. Tezduyar, and T. J. R. Hughes. Improving stability of stabilized and multiscale formulations in flow simulations at small time steps. *Computer Methods in Applied Mechanics and Engineering*, 199:828–840, 2010.

[61] C. Johnson. *Numerical solution of partial differential equations by the finite element method*. Cambridge University Press, Sweden, 1987.

[62] S.C. Brenner and L.R. Scott. *The Mathematical Theory of Finite Element Methods, 2nd ed.* Springer, 2002.

[63] A. Ern and J.-L. Guermond. *Theory and Practice of Finite Elements*. Springer, 2004.

[64] T.J.R. Hughes. Multiscale phenomena: Green's functions, the Dirichlet-to-Neumann formulation, subgrid scale models, bubbles, and the origins of stabilized methods. *Computer Methods in Applied Mechanics and Engineering*, 127:387–401, 1995.

[65] T.J.R. Hughes, G.R. Feijóo, L. Mazzei, and J.-B. Quincy. The variational multiscale method–A paradigm for computational mechanics. *Computer Methods in Applied Mechanics and Engineering*, 166:3–24, 1998.

[66] T.J.R. Hughes and G. Sangalli. Variational multiscale analysis: the fine-scale Green's function, projection, optimization, localization, and stabilized methods. *SIAM Journal of Numerical Analysis*, 45:539–557, 2007.

[67] K. Takizawa and T.E. Tezduyar. Multiscale space–time fluid–structure interaction techniques. *Computational Mechanics*, 48:247–267, 2011.

[68] T.E. Tezduyar, M. Behr, S. Mittal, and A. A. Johnson. Computation of unsteady incompressible flows with the finite element methods – space–time formulations, iterative strategies and massively parallel implementations. In *New Methods in Transient Analysis*, PVP-Vol.246/AMD-Vol.143, pages 7–24, New York, 1992. ASME.

[69] T. Tezduyar, S. Aliabadi, M. Behr, A. Johnson, and S. Mittal. Parallel finite-element computation of 3D flows. *Computer*, 26(10):27–36, 1993.

[70] A. A. Johnson and T.E. Tezduyar. Mesh update strategies in parallel finite element computations of flow problems with moving boundaries and interfaces. *Computer Methods in Applied Mechanics and Engineering*, 119:73–94, 1994.

[71] T.E. Tezduyar. Finite element methods for flow problems with moving boundaries and interfaces. *Archives of Computational Methods in Engineering*, 8:83–130, 2001.

[72] E. Oñate and F. Zarate. Rotation-free triangular plate and shell elements. *International Journal for Numerical Methods in Engineering*, 47:557–603, 2000.

[73] F. Cirak, M. Ortiz, and P. Schröder. Subdivision surfaces: a new paradigm for thin shell analysis. *International Journal for Numerical Methods in Engineering*, 47:2039–2072, 2000.

[74] F. Cirak and M. Ortiz. Fully C^1-conforming subdivision elements for finite deformation thin shell analysis. *International Journal for Numerical Methods in Engineering*, 51:813–833, 2001.

[75] F. Cirak, M. J. Scott, E. K. Antonsson, M. Ortiz, and P. Schröder. Integrated modeling, finite-element analysis, and engineering design for thin-shell structures using subdivision. *Computer-Aided Design*, 34:137–148, 2002.

[76] E. Oñate and F.G. Flores. Advances in the formulation of the rotation-free basic shell triangle. *Computer Methods in Applied Mechanics and Engineering*, 194:2406–2443, 2005.

[77] N. Nguyen-Thanh, J. Kiendl, H. Nguyen-Xuan, R. Wüchner, K.U. Bletzinger, Y. Bazilevs, and T. Rabczuk. Rotation-free isogeometric thin shell analysis using PHT-splines. *Computer Methods in Applied Mechanics and Engineering*, 200:3410–3424, 2011.

[78] J. Chung and G. M. Hulbert. A time integration algorithm for structural dynamics with improved numerical dissipation: The generalized-α method. *Journal of Applied Mechanics*, 60:371–75, 1993.

[79] K.E. Jansen, C.H. Whiting, and G.M. Hulbert. A generalized-α method for integrating the filtered Navier-Stokes equations with a stabilized finite element method. *Computer Methods in Applied Mechanics and Engineering*, 190:305–319, 2000.

[80] T.E. Tezduyar, S. Sathe, and K. Stein. Solution techniques for the fully-discretized equations in computation of fluid–structure interactions with the space–time formulations. *Computer Methods in Applied Mechanics and Engineering*, 195:5743–5753, 2006.

[81] T.E. Tezduyar, S. Sathe, R. Keedy, and K. Stein. Space–time finite element techniques for computation of fluid–structure interactions. *Computer Methods in Applied Mechanics and Engineering*, 195:2002–2027, 2006.

[82] T.E. Tezduyar and S. Sathe. Modeling of fluid–structure interactions with the space–time finite elements: Solution techniques. *International Journal for Numerical Methods in Fluids*, 54:855–900, 2007.

[83] U. Kuttler, C. Forster, and W. A. Wall. A solution for the incompressibility dilemma in partitioned fluid–structure interaction with pure Dirichlet fluid domains. *Computational Mechanics*, 38:417–429, 2006.

[84] K. Takizawa, C. Moorman, S. Wright, T. Spielman, and T.E. Tezduyar. Fluid–structure interaction modeling and performance analysis of the Orion spacecraft parachutes. *International Journal for Numerical Methods in Fluids*, 65:271–285, 2010.

[85] K. Takizawa, S. Wright, C. Moorman, and T.E. Tezduyar. Fluid–structure interaction modeling of parachute clusters. *International Journal for Numerical Methods in Fluids*, 65:286–307, 2010.

[86] H. Melbø and T. Kvamsdal. Goal oriented error estimators for Stokes equations based on variationally consistent postprocessing. *Computer Methods in Applied Mechanics and Engineering*, 192:613–633, 2003.

[87] E.H. van Brummelen, K.G. van der Zee, V.V. Garg, and S. Prudhomme. Flux evaluation in primal and dual boundary-coupled problems. *Journal of Applied Mechanics*, 79, 2012. 010904 (8pages).

[88] M.A. Scott. *T-splines as a Design-Through-Analysis Technology*. PhD thesis, The University of Texas at Austin, August 2011.